

June 1985

NASA-TP-2445 19850020637

# Piloted Simulation of an Algorithm for Onboard Control of Time-Optimal Intercept

Douglas B. Price,  
Anthony J. Calise,  
and Daniel D. Moerder

LIBRARY COPY

June 1985

ANALYSIS & RESEARCH CENTER  
LIBRARY COPY  
JUN 1985

3 1176 01311 2975

1985

# Piloted Simulation of an Algorithm for Onboard Control of Time-Optimal Intercept

Douglas B. Price  
*Langley Research Center  
Hampton, Virginia*

Anthony J. Calise  
*Drexel University  
Philadelphia, Pennsylvania*

Daniel D. Moerder  
*Information and Control Systems, Inc.  
Hampton, Virginia*



National Aeronautics  
and Space Administration

Scientific and Technical  
Information Branch



## CONTENTS

ABSTRACT .....	1
INTRODUCTION .....	1
SYMBOLS .....	2
PROBLEM STATEMENT .....	5
SINGULAR PERTURBATION FORMULATION .....	7
CONTROL SOLUTION IMPLEMENTATION .....	15
DESCRIPTION OF SIMULATION .....	21
CONCLUDING REMARKS .....	26
TABLES .....	28
FIGURES .....	29
APPENDIX - NON-PILOTED SIMULATION DATA FROM REFERENCE 2 .....	40
REFERENCES .....	44



## ABSTRACT

This paper describes a piloted simulation of algorithms for onboard computation of trajectories for time-optimal intercept of a moving target by an F-8 aircraft. The algorithms, which were derived using singular perturbation techniques, generate commands which are displayed to the pilot on the command bars of the attitude indicator in the cockpit. By centering the horizontal and vertical needles, the pilot flies an approximation to a time-optimal intercept trajectory. Several example simulations are shown and statistical data on the pilot's performance when presented with different display and computation modes are described.

## INTRODUCTION

From its beginning, NASA has had a very strong interest in aircraft trajectory control. As technology improves, the tools and techniques available to the control engineer also improve and allow more precise control of aircraft trajectories. The advent of computers that can be flown onboard the aircraft and used for solving flight control problems allows for onboard optimal control schemes that could not even be considered in the past. To take advantage of this new freedom, NASA began a program to apply singular perturbation techniques to study onboard optimal control of aircraft trajectories. Singular perturbation techniques allow a large numerical problem to be separated into a series of smaller subproblems that can be solved on small flight computers. The history of these techniques and their application to trajectory problems are described in references 1 and 2.

Singular perturbations were applied to the problem of time-optimal intercept of a moving target because that problem demonstrated the characteristics of the generic optimal control problem and was feasible for onboard implementation. Subsequent to a request for proposals for work in this area, two contracts were awarded. These contracts led to the general studies reported in references 1 and 2, and the more specific follow-up work included in reference 2. In reference 2, algorithms were derived for onboard control of time-optimal intercept of a moving target for an F-8 fighter aircraft. Computer simulations of the algorithms were included to demonstrate the techniques. The present paper describes the simulation of those algorithms on Langley's six-degree-of-freedom piloted simulation of the F-8 aircraft.

The intercept algorithms were programmed on Langley's real-time simulation system. The computer generated position and velocity coordinates for a target that was moving at a constant velocity. These algorithms can also be used to intercept maneuvering targets as long as the control solutions are updated frequently enough. The pilots who flew the simulated intercepts were all active Air Force or Air Force Reserve pilots who were currently flying either F-15 or F-106 aircraft.

The major purpose of the simulation described in this paper was to demonstrate the feasibility of onboard computation of time-optimal intercept trajectories. It was also undertaken to compare the different modes of computing the control inputs and presenting information to the pilot for use in the flight environment. This paper describes the complete problem statement and the algorithms used to compute the control inputs. The specifics of the simulation are discussed including the implementation of the algorithms and the methods of displaying the control information to

the pilots. The results of the piloted simulations are described and compared to demonstrate the feasibility of the different display modes. Sample time histories of the simulator output are shown and compared with the non-piloted simulations of reference 2. The results of a statistical analysis of the simulations are discussed and some conclusions are presented.

#### SYMBOLS

$A, B, C$	coefficients of quadratic equation for $\lambda_{Y4}$
$C_D$	drag coefficient
$C_{D,0}$	drag coefficient at zero lift
$C_{L_\alpha}$	lift curve slope
$D$	drag, N
$E$	total energy per unit weight, m
$E_S$	energy level at which zero-energy-rate boundary crosses $q_{\max}$ boundary, m
$G_{\max}$	maximum load factor
$g$	acceleration due to gravity, m/sec <sup>2</sup>
$H$	Hamiltonian function
$h$	altitude, m
$h_c(E, E_0)$	altitude along climb path as function of $E$ and $E_0$ , m
$h_d(E)$	altitude along descent path as function of $E$ , m
$J$	cost function for optimization problem
$K$	parameter in drag polar
$K_3$	constant used for computing thrust increments
$k$	multiplier for $\gamma$ -term in cost function
$L$	lift, N
$L_{13}$	vertical lift component for third boundary layer, N
$L_{14}$	vertical lift component for fourth boundary layer, N
$L_{1p}$	proportional vertical lift, N
$L_{22}$	horizontal lift component for second boundary layer, N
$L_{23}$	horizontal lift component for third boundary layer, N



$L_{24}$  horizontal lift component for fourth boundary layer, N  
 $M$  Mach number  
 $m$  mass of aircraft, kg  
 $q$  dynamic pressure,  $N/m^2$   
 $R$  range to target, m  
 $r_c(E, E_0)$  distance required to climb from  $E$  to  $E_0$ , m  
 $r_d(E)$  distance required to descend from  $E_0^*$  to  $E$ , m  
 $S$  aircraft reference area,  $m^2$   
 $s$  Laplace variable  
 $T$  thrust, N  
 $T_{mil}$  military thrust, N  
 $t$  time, sec  
 $t_c(E, E_0)$  time required to climb from  $E$  to  $E_0$ , sec  
 $t_d(E)$  time required to descend from  $E_0^*$  to  $E$ , sec  
 $t_{go}$  estimated time remaining until intercept, sec  
 $V$  true velocity, m/sec  
 $V_1$  velocity used to compute climb and descent paths, m/sec  
 $W$  aircraft weight, N  
 $X, Y$  horizontal plane coordinates for ground track plots (figs. 8 and 11), m  
 $x, y$  position of F-8 relative to target (fig. 1), m  
 $\alpha$  angle of attack, rad  
 $\beta$  heading, rad  
 $\gamma$  flight-path angle, rad  
 $\gamma_D$  desired flight-path angle  
 $\delta( )$  increment in ( )  
 $\varepsilon$  parameter used to scale state equations for singular perturbations  
 $\zeta$  damping ratio of second-order system used for proportional lift control  
 $\eta$  induced drag parameter

$\lambda$	angle-of-sight line to target
$\lambda_{x_0}$	costate for state variable $x$
$\lambda_{y_0}$	costate for state variable $y$
$\lambda_{E_1}$	costate for state variable $E$
$\lambda_{\beta_2}$	costate for state variable $\beta$
$\lambda_{h_3}$	costate for state variable $h$
$\lambda_{\gamma_4}$	costate for state variable $\gamma$
$\mu$	bank angle, rad
$\rho$	air density, $\text{kg/m}^2$
$\tau$	scaled time variable
$\tau_1, \tau_2$	time constants used for proportional control for vertical lift
$\phi$	parameter used to solve for $\lambda_{\gamma_4}$
$\omega_n$	undamped natural frequency of second-order system used for proportional lift control, rad/sec

#### Subscripts:

c	climb
d	descent
f	final
max	maximum
min	minimum
o	outer layer
T	target
0	initial
1	first boundary layer
2	second boundary layer
3	third boundary layer

#### Superscripts:

$(\cdot)$	derivative with respect to time
*	optimal cruise conditions

# PROBLEM STATEMENT

The particular problem chosen to demonstrate the feasibility of onboard trajectory optimization is the minimum-time intercept of a moving target. It is assumed that the initial time is fixed and given but that the final time is free and occurs at target intercept. The objective function for this study is

$$J = \int_{t_0}^{t_f} (1 + k \sin^2 \gamma) dt \quad (k > 0) \quad (1)$$

The second term in the cost function penalizes the oscillation in altitude and flight-path angle caused by separating those two states in the singular perturbation formulation of the problem. A minimum-time problem results when  $k$  is set to zero. The choice of the parameter  $k$  is discussed in references 2 and 3.

The state equations for the F-8 aircraft considered as a point mass are as follows:

$$\left. \begin{aligned} \dot{x} &= V \cos \gamma \cos \beta \\ \dot{y} &= V \cos \gamma \sin \beta - V_T \cos \gamma_T \\ \dot{E} &= \frac{(T - D)V}{W} \\ \dot{\beta} &= \frac{L \sin \mu}{mV \cos \gamma} \\ \dot{h} &= V \sin \gamma \\ \dot{\gamma} &= \frac{L \cos \mu - W \cos \gamma}{mV} \end{aligned} \right\} \quad (2)$$

The variables in equations (2) are defined with the aid of figure 1, where the subscript  $T$  is used to designate the target. These equations are valid for a flat Earth, thrust ( $T$ ) directed along the flight path, and constant weight ( $W$ ). Drag is assumed to have the parabolic form

$$D = qSC_D = qS(C_{D,o} + \eta C_{L,\alpha}^2) \quad (3)$$

which can also be written as

$$D = qSC_{D,o} + \frac{KL^2}{qS} \quad (4)$$

where the dynamic pressure  $q = \rho V^2/2$ ,  $\rho$  is the air density, and

$$K = \frac{\eta}{C_{L_\alpha}} \quad (5)$$

$$L = qSC_L = qS(C_{L_\alpha} \alpha) \quad (6)$$

The variable  $E$  is the total aircraft energy (kinetic and potential) per unit weight:

$$E = h + \frac{V^2}{2g} \quad (7)$$

where  $h$  is the aircraft altitude. The control variables are aircraft lift ( $L$ ), bank angle ( $\mu$ ), and thrust ( $T$ ).

The minimization of the objective function (eq. (1)) is subject to the following state and control variable constraints:

$$L \leq WG_{\max} \quad (8)$$

$$L \leq qSC_{L_\alpha} \alpha_{\max} \quad (9)$$

$$T_{\min}(h,V) \leq T \leq T_{\max}(h,V) \quad (10)$$

$$q \leq q_{\max} \quad M \leq M_{\max}(h) \quad (11)$$

where  $G_{\max}$  is the maximum load factor,  $\alpha_{\max}$  is the stall angle of attack, and  $T_{\min}$  and  $T_{\max}$  are the minimum and maximum thrust levels, which are functions of aircraft altitude ( $h$ ) and velocity ( $V$ ). The Mach limit is included for completeness.

However, it was never encountered in the simulations. The boundary conditions are such that the initial aircraft state is fully specified and intercept is defined by

$$x(t_f) = y(t_f) = 0 \quad h(t_f) = h_T(t_f) \quad (12)$$

where  $h_T(t_f)$  is taken as the projected target altitude

$$h_T(t_f) = h_T(0) + (V_T \sin \gamma_T) t_f \quad (13)$$

#### SINGULAR PERTURBATION FORMULATION

The solution of an optimal control problem generally involves solving a two-point boundary value problem (TPBVP). The control solution thus obtained is a function of time and the initial and terminal conditions. In theory, a useful feedback law could be obtained by periodically updating the solution of the TPBVP and basing the boundary conditions on the current system state. However, for dynamics of even modest complexity, numerically updating the TPBVP requires more time and core memory than are compatible with implementation onboard an aircraft. Thus, for such an application, simplifying approximations must be introduced into the control problem formulation.

Aircraft dynamics are characterized by the presence of states whose speeds are widely separated. Singular perturbation theory (SPT) is well suited to treat systems such as this, which have a mixture of quick and slower motions. The application of SPT to these systems can generate approximate solutions to high-order optimal control problems which perform nearly as well as the complete solutions and are simpler to derive and implement.

A singularly perturbed system is represented with small parameters scaling the fast state derivatives. These parameters normally represent "parasitic" phenomena: small time constants, masses, and so forth. The SPT approximation consists of setting these small parameters to zero, and thus decomposing the dynamics into separate "slow" and "fast" subsystems. This is advantageous for two reasons. First, it breaks the original control problem into subproblems of lower dimension. Second, while the wide separation of the state velocity magnitudes in the original problem rendered it numerically ill-conditioned, the subproblems are well-conditioned. The solutions of these subproblems, when reassembled, approximate the solution of the original control problem. A comprehensive survey of SPT in control theory is found in reference 4.

In the present study a small parameter,  $\epsilon$ , is introduced into the dynamics, with successively faster state derivatives multiplied by successively higher powers of  $\epsilon$ . Ideally,  $\epsilon$  would be identified with a particular system parameter, as in references 5, 6, and 7. Here, however,  $\epsilon$  is merely "small," and the ordering of states with respect to speed is based on familiarity with the F-8 aircraft dynamics and knowledge of the type of trajectories associated with minimum-time intercepts. This approach, employed in references 1-3, 8, and 9, is often called "forced singular perturbations." While the ordering of dynamics used here corresponds to that used in references 2, 3, and 8, examples of other orderings appear in references 1 and 7. References 2 and 3 discuss the rationale for the separation of altitude and

flight-path angle dynamics and compare some results for a vertical plane analysis of motions with and without the separation.

The state equations scaled by powers of  $\epsilon$  are as follows:

$$\left. \begin{aligned} \dot{x} &= V \cos \gamma \cos \beta \\ \dot{y} &= V \cos \gamma \sin \beta - V_T \cos \gamma_T \\ \epsilon \dot{E} &= \frac{(T - D)V}{W} \\ \epsilon^2 \dot{\beta} &= \frac{L \sin \mu}{mV \cos \gamma} \\ \epsilon^3 \dot{h} &= V \sin \gamma \\ \epsilon^4 \dot{\gamma} &= \frac{L \cos \mu - W \cos \gamma}{mV} \end{aligned} \right\} \quad (14)$$

The first reduced-order problem, called the outer layer, is formulated by setting  $\epsilon = 0$  in the equations of motion (eqs. (14)). This makes the left-hand sides of the last four state equations zero, changing them from differential equations into algebraic equations. Under the assumption of constant target velocity, the resulting system can be solved for the cruise energy that should be used for a time-optimal intercept. If the projected distance to the intercept point is sufficiently large, the optimal cruise point for the aircraft is the solution to the outer layer problem. If the projected distance is not large enough for the aircraft to climb efficiently to that energy before intercept, then a lower altitude-energy combination is chosen as the outer layer solution. The logic used for this part of the solution will be described in a later section.

The remaining reduced-order problems that are used to approximate the solution are called boundary layers and are derived by changing the independent variable for the differential equations from  $t$  to  $\tau = t/\epsilon^i$ , where  $i$  is the power of  $\epsilon$  on the left-hand side of the differential equation that describes the dynamics of interest. For example, the first boundary layer is obtained by scaling the independent variable by  $1/\epsilon$ , which changes the set of differential equations from equations (14) to a similar set with the powers of  $\epsilon$  reduced by one in each equation. This has the effect of multiplying the right-hand sides of the first two equations by  $\epsilon$  and removing  $\epsilon$  completely from the third (E) equation. When  $\epsilon$  is set to zero, there remains only the one differential equation for  $E$  to solve, with  $x$  and  $y$  assumed to be constant at the values used in the last iteration of the outer solution. The solution to this first boundary layer subproblem gives the so-called energy climb path that describes an ideal energy trajectory from the initial condition to the cruise energy defined by the outer layer solution.

The remaining subproblems (boundary layers) are derived by successive rescalings of the independent variable to isolate the individual state differential equations so that each may be solved separately. At the end of this process, equations for the control variables in terms of the current values of the state variables are achieved. This gives the desired feedback control law. Each of the separate subproblem solutions will be discussed in more detail in later sections of the paper.

Singular perturbation techniques simplify the problem when the required assumptions are valid, even if each state equation cannot be isolated from all the others. However, if more than one equation is being solved on the same time scale, in general, a two-point boundary value problem must be solved. This precludes generating a solution in real time onboard the aircraft. The special case of the first two state equations for this problem can be solved on one time scale because of extra information supplied by the geometry of the intercept formulation along with the assumption of constant target velocity at each step.

### Outer Layer

The outer layer subproblem, generated by setting  $\epsilon$  to zero in equations (14), has only the two state equations for  $\dot{x}$  and  $\dot{y}$ . Since the target velocity is assumed to be constant, the subproblem consists of solving for an optimal intercept in the horizontal plane. Even though there are two state equations, it is not necessary to solve a two-point boundary value problem for the solution because there is extra geometric information generated by the necessity of intercept with the target. This condition is given by

$$V \sin(\beta - \lambda) = V_T \cos \gamma_T \cos \lambda \quad (15)$$

where  $\lambda$  is the angle-of-sight line to the target. The control variables for the outer layer are  $h$  and  $E$  and are given by

$$h_0, E_0 = \arg \max_{h, E} (V) \quad (16)$$

Thrust equals drag and lift equals weight for the outer layer. Bank angle and flight-path angle are both zero:

$$T_0 = D_0 \quad \mu_0 = 0 \quad \gamma_0 = 0 \quad L_0 = W \quad (17)$$

For  $L = W$ , the drag is

$$D_0 = q S C_{D,0} + \frac{KW^2}{qS} \quad (18)$$

where

$$q = \frac{\rho(h)v_o^2}{2} \quad (19)$$

$$v_o = \sqrt{2g(E_o - h_o)} \quad (20)$$

The cruise solution in the vertical plane is independent of target motion and intercept geometry. It depends only on the projected intercept point. The optimal heading  $\beta_o$  and the costates  $\lambda_{x_o}$  and  $\lambda_{y_o}$  resulting from the Hamiltonian formulation of the problem are the only variables that must be computed on-line:

$$\beta_o = \sin^{-1}\left(\frac{v_T}{v_o} \cos \gamma_T \cos \lambda\right) + \lambda \quad (21)$$

$$\lambda_{x_o} = \frac{-\cos \beta_o}{v_o - v_T \cos \gamma_T \sin \beta_o} \quad (22)$$

$$\lambda_{y_o} = \frac{-\sin \beta_o}{v_o - v_T \cos \gamma_T \sin \beta_o} \quad (23)$$

Equation (16) for the optimal energy is valid only if there is sufficient range between the aircraft and the target to allow the aircraft to reach that energy prior to intercept. In case the range to the target is not large enough, a lower outer layer energy is chosen. This procedure is described in the section on control system implementation.

#### First Boundary Layer

The first boundary layer subproblem is generated by changing the independent variable  $t$  in equations (14) to  $\tau = t/\epsilon$  and then letting  $\epsilon$  approach zero. This leaves only the two differential equations for energy  $E$  and its costate  $\lambda_{E_1}$ . The remaining state and costate equations all reduce to algebraic equations and give the constraints,

$$\mu_1 = 0 \quad \gamma_1 = 0 \quad L_1 = W \quad (24)$$



The control variables for the first boundary layer are  $T$ ,  $h$ , and  $\beta$ . The optimal heading ( $\beta_1$ ) is the same as that for the outer layer. Since  $T$  appears linearly in the equations, optimal thrust is given by the two equations,

$$T_1 = T_{\max}(h_1, V_1) \quad (\lambda_{E_1} < 0) \quad (25)$$

$$T_1 = T_{\min}(h_1, V_1) \quad (\lambda_{E_1} > 0) \quad (26)$$

These equations mean that thrust is maximized during climb and minimized during descent. The optimal altitude for the first boundary layer also has two separate equations corresponding to climb and descent:

$$h_1 = \arg \min_h \left[ \frac{(T_{\max} - D_o)V}{V - V_o} \right] \bigg|_{\substack{E=E_{\text{current}} \\ T>D \text{ (climb)}}} \quad (27)$$

$$h_1 = \arg \min_h \left[ \frac{-(T_{\min} - D_o)V}{V - V_o} \right] \bigg|_{\substack{E=E_{\text{current}} \\ T<D \text{ (descent)}}} \quad (28)$$

The climb path to the optimal cruise point can be seen in figure 2. The descent path follows the  $q_{\max}$  boundary. The costate for the first boundary layer is given by

$$\lambda_{E_1} = \frac{-WH_o(E, h_1)}{V_1(T_1 - D_o)} \quad (29)$$

where  $H_o(E, h_1)$  is the Hamiltonian for the outer solution evaluated at the first boundary conditions:

$$H_o(E, h_1) = [\lambda_{x_o} V \cos \beta_o + \lambda_{y_o} (V \sin \beta_o - V_T \cos \gamma_T) + 1] \bigg|_{\substack{E=E_{\text{current}} \\ h=h_1}} \quad (30)$$

The solution for  $h_1(E)$  is independent of target motion and can be precomputed and stored as a function of  $E$ . Only the costate  $\lambda_{E_1}$  must be computed on-line.

## Second Boundary Layer

The second boundary layer is obtained by setting  $\tau = t/\epsilon^2$  and letting  $\epsilon$  approach zero. This results in the constraints,

$$\gamma_2 = 0 \quad L^2 = L_{22}^2 + W^2 \quad (31)$$

where  $L$  is the total lift and  $L_{22}$  is the horizontal lift component. The control variables in this boundary layer are  $T$ ,  $h$ , and  $L_{22}$ . The state variable  $\beta$  is considered a faster variable than energy (eqs. (14)), so all turning is assumed to take place near the initial time where  $\lambda_{E_1} < 0$ . Then the optimal thrust is

$$T_2 = T_{\max}(h_2, V_2) \quad (32)$$

where  $h_2$  is defined by

$$h_2 = \arg \min_h \left[ \frac{-\rho}{KVH_1(E, h, \beta)} \right] \bigg|_{\substack{E=E_{\text{current}} \\ \beta=\beta_{\text{current}}}} \quad (33)$$

and  $H_1(E, h, \beta)$  is the first boundary layer Hamiltonian evaluated at current values of  $E$ ,  $h$ , and  $\beta$ . It is expressed as

$$H_1(E, h, \beta) = \lambda_{x_0} V \cos \beta + \lambda_{y_0} (V \sin \beta - V_T \cos \gamma_T) + \lambda_{E_1} \frac{(T - D_0)V}{W + 1} \quad (34)$$

The solution for  $L_{22}$  is analytic and is given by

$$L_{22} = \sqrt{-qSWH_1(E, h, \beta)/VK\lambda_{E_1}} \quad \text{sign}(\beta_0 - \beta) \quad (35)$$

After the minimization in equation (33) is performed, the heading costate variable is computed from

$$\lambda_{\beta_2} = -2H_1(E, h, \beta) \frac{mV}{L_{22}} \bigg|_{h=h_2} \quad (36)$$

The calculations in the above equations must be performed on-line. To accelerate the minimization for  $h_2$  from equation (33), the solution from the previous time instant is used as a starting point. This calculation is performed each time the control solution is updated.

### Third Boundary Layer

The third boundary layer addresses the altitude dynamics. The equations are derived by introducing the transformation  $\tau = t/\epsilon^3$  and letting  $\epsilon$  approach zero. The vertical lift  $L_{13}$  for this boundary layer is

$$L_{13} = W \cos \gamma_3 \quad (37)$$

Because  $\gamma$  can be nonzero, the penalty term  $k \sin^2 \gamma$  in the cost function (eq. (1)) has an effect on the solution for the third and fourth boundary layers. The control variables here are horizontal lift  $L_{23}$  and  $\gamma_3$ . The zero-order solution for  $L_{23}$  is given by

$$L_{23} = \min \left\{ L_{2\max}, L_{22}/\cos \gamma_3 \right\} \quad (38)$$

where

$$L_{2\max} = \sqrt{L_{\max}^2 - L_{13}^2} \quad (39)$$

It can be seen that  $L_{23}$  approaches  $L_{22}$  as  $\gamma_3$  approaches zero, which is the constrained value for  $\gamma$  in the second boundary layer. The expression for  $\gamma_3$  is

$$\gamma_3 = \arg \max_{\gamma} [\sin \gamma / H_2(h, E, \beta, \gamma)] \operatorname{sign}(h_2 - h) \quad (40)$$

where  $H_2$  is the second boundary layer Hamiltonian evaluated at the current conditions for its arguments:

$$\begin{aligned} H_2(h, E, \beta, \gamma) = & (\lambda_{x_0} \cos \beta + \lambda_{y_0} \sin \beta) V \cos \gamma - \lambda_{y_0} V_T \cos \gamma_T \\ & + \lambda_{E_1} \frac{(T - D)V}{W} + \lambda_{\beta_2} \frac{L_{23}g}{WV \cos \gamma} + 1 + k \sin^2 \gamma \end{aligned} \quad (41)$$

The costate for this boundary layer  $\lambda_{h_3}$  is determined from

$$\lambda_{h_3} = \frac{-H_2(h, E, \beta, \gamma_3)}{V \sin \gamma_3} \quad (42)$$

To determine  $L_{23}$  in equation (41), equation (38) is evaluated at the search value for  $\gamma$  in equation (40). All the calculations in this layer must be performed on-line.

#### Fourth Boundary Layer

The equations for the fourth boundary layer are defined by using the time transformation  $\tau = t/\varepsilon^4$  and again letting  $\varepsilon$  approach zero. In this layer, the vertical and horizontal components of lift ( $L_{14}$  and  $L_{24}$ , respectively) are refined to reflect the flight-path angle dynamics. As long as  $L < L_{\max}$ , the lift components are

$$L_{14} = W \cos \gamma + \left[ -H_3(h, E, \beta, \gamma) \frac{qSW}{\lambda_{E_1} KV^2} - (L_{24} - L_{23})^2 \right]^{1/2} \text{sign}(\gamma_3 - \gamma) \quad (43)$$

$$L_{24} = \lambda_{\beta_2} \frac{qgS}{2\lambda_{E_1} KV^2 \cos \gamma} \quad (44)$$

These are used to define the final lift and bank angle commands:

$$L = \sqrt{L_{14}^2 + L_{24}^2} \quad (45)$$

$$\mu = \tan^{-1} \left( \frac{L_{24}}{L_{14}} \right) \quad (46)$$

If  $L$  (defined above) exceeds  $L_{\max}$ , we set  $L = L_{\max}$  and obtain an expression for bank angle  $\mu$ :

$$\tan \mu = \left( \frac{\lambda_{\beta_2}}{\lambda_{\gamma_4} \cos \gamma} \right) \text{sign}(\beta_o - \beta) \quad (47)$$

In this formulation  $\lambda_{\gamma_4}$ , the costate for  $\gamma$ , is evaluated as a root of

$$A\lambda_{\gamma_4}^2 + B\lambda_{\gamma_4} + C = 0 \quad (48)$$

where

$$A = \frac{g^2 (L_{\max}^2 / w^2 - \cos^2 \gamma)}{v^2} \quad (49)$$

$$B = 2\phi \cos \gamma g/v \quad (50)$$

$$C = \left( \frac{\lambda_{\beta_2} L_{\max} g}{wv \cos \gamma} \right)^2 - \phi^2 \quad (51)$$

$$\phi = H_1 - \lambda_{E_1} \frac{(L_{\max}^2 - w^2 \cos^2 \gamma)KV}{qSW} + \lambda_{h_3} v \sin \gamma \quad (52)$$

The equation for  $\lambda_{\gamma_4}$  always has real roots of opposite sign; thus  $\lambda_{\gamma_4}$  is chosen such that

$$\text{sign}(\lambda_{\gamma_4}) = -\text{sign}(\gamma_3 - \gamma) \quad (53)$$

Given this value for  $\lambda_{\gamma_4}$ , bank angle  $\mu$  is computed from equation (47) with  $\mu$  placed in the quadrant appropriate to  $\text{sign}(\gamma_3 - \gamma)$ . It should be noted that the arbitrary separation of  $h$  and  $\gamma$  dynamics in the third and fourth boundary layers fails to account for the coupling that naturally exists between these states. Reference 2, appendix D, shows a method for choosing  $k$  in the cost function so that this problem is alleviated.

#### CONTROL SOLUTION IMPLEMENTATION

This section describes the feedback implementation of the control solution formed from the singular perturbation outer and boundary layer solutions described in the previous sections. Five topics are covered: organization of climb and descent legs, an alternate proportional vertical lift scheme, thrust and lift control during descent, avoidance of singularities in the control solution, and the overall organization of the actual feedback implementation.

## Climb and Descent Legs

If initial turning and other transients are ignored, long-range intercept trajectories have three stages. The first stage is a climb to cruise at the long-range optimal cruise energy ( $E_o^*$ ). The second stage is a cruise leg. The third stage can take one of two forms. If the target altitude is below the altitude for long-range cruise, it is a descent leg. If the target altitude is above the long-range cruise altitude, the terminal stage is a zoom climb (constant-energy altitude gain) maneuver. It is important to note that climb and descent in this paper refer to gain and loss of energy - not altitude. For example, altitude decreases during a portion of the climb profile.

Short-range intercepts are defined as occurring when the intercept range is less than the range required to fly a long-range climb and descent. In this case, the optimal trajectory would consist of climb and descent legs that meet at an energy level less than  $E_o^*$  at an altitude and velocity on the zero-energy-rate boundary for  $T = T_{\max}$ , or on the dynamic pressure or Mach constraint boundaries. (Henceforth, these lower energy cruise conditions will be referred to as pseudo-cruise points,  $E_o$ .) As in the case of long-range cruise, climb and descent paths meeting at  $E_o < E_o^*$  are obtained from the first boundary layer altitude solutions (eqs. (27) and (28)) and are functions of  $V_o(E_o)$ , which permits them to be calculated off-line. An example climb path to a pseudo-cruise energy is illustrated in figure 2. Reference 2 displays climb altitude profiles for the F-8 aircraft as functions of energy for several values of  $E_o$ .

An important element in the control design is the decision logic which determines whether an intercept path is long- or short-range. When a short-range intercept is identified, the logic must select an appropriate value of  $E_o$ . Ideally,  $E_o$  would be chosen so that the horizontal range for climb and descent matches the predicted intercept range. In the control solution implementation, optimal climb and descent altitude schedules for a number of discrete values of  $E_o$  are precomputed and stored in the form  $h_c(E, E_o)$  for climb and  $h_d(E)$  for descent. The descent profiles are independent of  $E_o$  because the optimal descent paths lie on the dynamic pressure boundary. Given this discretization of the first boundary layer solution as a function of  $E_o$ , the range-matching task becomes a matter of choosing the highest value of  $E_o$  such that the horizontal range for climb and descent is less than or equal to the predicted intercept range. When the inequality is strict, a cruise leg at  $E_o$  is traversed before initiating descent. Descent is initiated when the horizontal range for descent from  $E_o$  matches the predicted range to intercept.

The time  $t_c(E, E_o)$  and horizontal distance  $r_c(E, E_o)$  required to climb from  $E$  to  $E_o$  are determined by computing the integrals,

$$t_c(E, E_o) = \int_E^{E_o} \frac{1}{\dot{E}} dE \quad (54)$$

$$r_c(E, E_o) = \int_E^{E_o} \frac{V_1}{\dot{E}} dE \quad (55)$$

where

$$v_1 = \sqrt{[E - h_1(E, E_0)]2g} \quad (56)$$

and  $\dot{E}$  is the energy rate computed at  $h_c(E, E_0)$ . Tabular data for  $h_c(E, E_0)$ ,  $t_c(E, E_0)$ , and  $r_c(E, E_0)$  is presented in reference 2 for the F-8 aircraft at  $E_0^*$  and several pseudo-cruise energies.

The expressions used in calculating altitude and range for descent differ slightly from those used in calculating altitude and range for climb. During descent, the rapid rise in the rate of closure, normalized with respect to remaining range, causes the terminal miss distance to become highly sensitive to error in the remaining range estimate; thus,

$$t_d(E) = \int_{E_0^*}^{E_0} \frac{1}{\dot{E}} dE \quad (57)$$

$$r_d(E) = \int_{E_0^*}^{E_0} \frac{\dot{r}_d}{\dot{E}} dE \quad (58)$$

where

$$\dot{r}_d = v_1 \cos \gamma_d \quad (59)$$

$$v_1 = \sqrt{[E - h_d(E)]2g} \quad (60)$$

$$\gamma_d = \sin^{-1} \left[ \frac{(\dot{h}_d/dE) \dot{E}}{v_1} \right] \quad (61)$$

where  $E$  is the energy at initiation of descent. Tabular values for  $h_d(E)$ ,  $t_d(E)$ , and  $r_d(E)$  are provided in reference 2 for the F-8 aircraft.

Climb times and ranges from the current energy to the cruise energy are obtained by interpolating and differencing the values in the tables of reference 2. A similar procedure is used for descent. For example,

$$t_d(E, E_f) = t_d(E_f) - t_d(E) \quad (62)$$

$$r_d(E, E_f) = r_d(E_f) - r_d(E) \quad (63)$$

In general,  $E_f$  is not known a priori and must be determined such that  $h(t_f) = h_T(t_f)$ . A terminal constraint must be satisfied:

$$h_d(E_f) = h_T + V_T \sin \gamma_T t_{go} \quad (64)$$

where  $t_{go}$  is the estimated time remaining until intercept. Referring to the intercept geometry in figure 1, descent is initiated when

$$r_d(E_o, E_f) \cos(\beta_o - \lambda) > R + (V_T \cos \gamma_T \sin \lambda) t_d(E_o, E_f) \quad (65)$$

is satisfied, where  $R$  is the current horizontal range.

#### Proportional Vertical Lift

An option was included in the control logic for stopping the singular perturbation solution after the second boundary layer and using a suboptimal proportional control for vertical lift. This option was included to investigate the sensitivity of the solution to the final two boundary layers. Also, the proportional control is computationally easier to implement than the full singular perturbation solution. First the desired flight-path angle is defined by

$$\gamma_D = \frac{h_2 - h_1}{\tau_1 V} + \frac{\dot{E}}{V_1} \frac{dh_1}{dE} \quad (66)$$

where  $V_1 = \sqrt{(E - h_1)2g}$ . The second term in the above equation is an approximation to the flight-path angle for following the first boundary layer climb path. The proportional vertical lift ( $L_{1p}$ ) is computed based on a desired flight-path angle rate proportional to  $(\gamma_D - \gamma)$ :

$$\dot{\gamma}_D = \frac{\gamma_D - \gamma}{\tau_2} = \frac{L_{1p} - W \cos \gamma}{mV} \quad (67)$$

Solving for  $L_{1p}$ , we have

$$L_{1p} = mV \frac{\gamma_D - \gamma}{\tau_2} + W \cos \gamma \quad (68)$$



The control variables, total lift  $L$  and bank angle  $\mu$ , are then computed as

$$L = \sqrt{L_{1p}^2 + L_{22}^2} \quad (69)$$

$$\mu = \tan^{-1}\left(\frac{L_{22}}{L_{1p}}\right) \quad (70)$$

A block diagram of these calculations is given in figure 3. The characteristic equation for the resulting transfer function is

$$\tau_1 \tau_2 s^2 + \tau_1 s + 1 = 0 \quad (71)$$

where  $s$  is the Laplace variable. The undamped natural frequency ( $\omega_n$ ) and the damping ratio ( $\zeta$ ) for this second-order system are

$$\omega_n = \frac{1}{\sqrt{\tau_1 \tau_2}} \quad (72)$$

$$\zeta = \frac{\sqrt{\tau_1 / \tau_2}}{2} \quad (73)$$

The values chosen for the F-8 aircraft were  $\omega_n = 0.1$  rad/sec and  $\zeta = 0.8$ , resulting in values for  $\tau_1$  and  $\tau_2$  of 15.0 and 6.0 sec, respectively. The choice of  $\omega_n$  and  $\zeta$  was made on the basis of an eigenvalue analysis of the optimal  $h$  and  $\gamma$  dynamics over a range of energy levels, documented in appendix D of reference 2.

#### Thrust and Lift Control During Descent

In the ideal case of a fully optimal control solution, there would be insignificant maneuvering and throttle variation during descent. There is, however, significant turning in the solution implemented, primarily because of two factors. First, since the aircraft follows the dynamic pressure constraint boundary during most of the descent and since the flight-path angle is nonzero, the intercept heading changes from the optimal cruise heading value. Thus, it is necessary to update the intercept heading during descent using the equation for the optimal heading  $\beta_o$ , from the outer layer, and the horizontal component of aircraft velocity. Second, target maneuvers that occur after the initiation of descent necessitate heading changes. The former problem could be greatly reduced by correcting the outer solution to first order in  $\epsilon$ , in a manner similar to the procedure followed in reference 9.

In order to ensure intercept under all conditions, both thrust and  $L_{22}$  must be modulated during descent. In the case of  $L_{22}$ , maximum lift should always be used during descent in maintaining the intercept heading, because  $\lambda_{E_1}$  becomes positive. In practice, small heading errors are nulled by a proportional control law. Further, during descent, the vertical lift command is obtained through the previously described proportional control option.

Thrust modulations are used to control rate of descent to ensure that  $h = h_T$  at intercept. Two correction terms are introduced:

$$T = T_d + \delta T_1 + \delta T_2 \quad (74)$$

where  $T_d$  is the nominal descent thrust from the first boundary layer. The second term corrects for the fact that  $L$  does not equal  $W$  during descent, since this is assumed in generating the  $t_d$  and  $r_d$  tabular data. Thus,  $\delta T_1$  compensates for the increased drag caused by lift variations:

$$\delta T_1 = \frac{K(L^2 - W^2)}{qS} \quad (75)$$

The third term in equation (74) compensates for the current mismatch ( $\delta R$ ) in range, where we replace  $E_o$  by  $E$  in the equation for initiating descent to get

$$\delta R = R + (V_T \cos \gamma_T \sin \lambda) t_d(E, E_f) - r_d(E, E_f) \cos(\beta_o - \lambda) \quad (76)$$

A proportional control law was derived by defining

$$\dot{\delta R} = -K_3 \delta R \quad (77)$$

Noting that

$$\dot{\delta R} = \frac{dr_d(E, E_f)}{dE} \cos(\beta_o - \lambda) \dot{\delta E} \quad (78)$$

$$\dot{\delta E} = \frac{\delta T_2 V}{W} \quad (79)$$

one can solve for  $\delta T_2$  as

$$\delta T_2 = \frac{K_3 W \delta R}{V \cos(\beta_o - \lambda) [dr_d(E, E_f)/dE]} \quad (80)$$

In order to allow for thrust variation,  $T_{\min}$  was set equal to  $T_{\text{mil}}/2$ , where  $T_{\text{mil}}$  is the military thrust level.

It should be noted that a portion of the descent path calls for  $T_d = T_{\max}$ . Referring to figure 4, note that upon initiating descent, for  $E_o > E_s$ , the commanded altitude on the descent path is such that  $V_1(E_o) > V_o(E_o)$ . As shown in appendix A of reference 2, this means that  $\lambda_E$  remains negative until  $V_1(E) < V_o(E_o)$ , which from the first boundary layer solution implies that  $T = T_{\max}$ .

### Summary of Control Calculations

The control calculations including both proportional vertical lift and calculations for the full zero-order solution are summarized in figure 5. All on-line calculations are referenced by equation numbers. The purpose of the range-matching block is to establish the proper cruise or pseudo-cruise energy level  $E_o$ . During climb, the costates are calculated on-line and  $h_c(E, E_o)$  is taken from tabular data. All turn parameters are calculated on-line. During descent,  $h_d(E, E_f)$  is drawn from tabular data, and thrust and lift are calculated as described in the previous section.

### Avoiding Numerical Singularities

Numerical difficulties evidenced by discontinuities in the control solution were encountered when the aircraft altitude, heading, and/or flight-path angle approached their optimal values for the second and third boundary layer solutions. These discontinuities occurred when certain functions approached an indeterminate form as the optimum state values were approached. For example, the argument being minimized in the second boundary layer equation for  $h_2$  approaches an indeterminate form as heading error approaches zero. The corrective measures took the form of first-order Taylor series expansions and approximations taking advantage of the asymptotic character of the boundary layer solutions. A more detailed description is given in appendix F of reference 2.

### DESCRIPTION OF SIMULATION

The F-8 aircraft was chosen for this simulation because of the availability of a very realistic simulation of NASA's Digital Fly-by-Wire (DFBW) aircraft, which is an F-8C modified so that the only link between the pilot and the aerodynamic control surfaces is through the onboard digital computer. The level flight envelope of the DFBW aircraft is shown in figure 2. The zero-energy-rate contour defines the limits of level steady-state flight with full thrust and afterburner. This contour, the dynamic pressure limit below an altitude of 5100 m, and the maximum angle of attack boundary at low speed define the envelope for steady-state flight.

The Langley simulation of the DFBW aircraft uses a complete six-degree-of-freedom model that accurately represents the aircraft throughout its flight envelope. This software resides on Langley's real-time digital simulation system consisting of several Control Data Corporation (CDC) 6000 series and CYBER 175 computers and associated analog and digital interfaces.<sup>1</sup>

The cockpit used for the simulation is a general purpose fixed-base cockpit used at Langley to represent various types of aircraft from small general aviation airplanes to the Space Shuttle. For the F-8 simulation, this cockpit had the standard instrumentation necessary for determining aircraft attitude, velocity, acceleration, angle of attack, and sideslip angle. A schematic of the instrument panel is shown in figure 6. The rudder pedals were standard for a jet fighter, the throttle was from an actual F-8 cockpit, and the stick was a sidearm stick with force rather than displacement transducers.

The information generated by the optimal trajectory algorithms was presented to the pilot by flight director needles (command bars) on the attitude indicator at the center of the instrument panel. The pilot's task was to keep both horizontal and vertical needles centered in order to remain on the optimal intercept trajectory. In addition, the pilot modulated the throttle during descent to null a display indicating desired thrust.

A number of flights were simulated by the authors to determine the characteristics of the algorithms and to verify that a pilot could actually fly as directed by the displays and achieve an intercept. These preliminary flights also served to check a number of possible test cases for use by the professional pilots in the second phase of the study. For the part of the simulation flown by the pilots, three initial conditions were selected to represent possible situations for two aircraft. The pilots were told to fly the simulator so that the needles remained centered in order to intercept a computer-generated target. The set of initial conditions flown by the pilots was chosen to require the algorithms to generate flight paths that the pilots might fly themselves. This allowed the pilots to comment on what the algorithms told them to do in relation to what they would do themselves under similar circumstances.

The three sets of initial conditions are illustrated in figure 7. For case 1, the target aircraft was 46 736 m ahead and 26 924 m to the right of the F-8 and flying at about a 60° angle with respect to the F-8's flight path. Both the F-8 and the target were at an initial altitude of 3048 m. The target flew at a constant velocity at Mach 0.71. The F-8 was initially at Mach 0.9. Case 2 differed from case 1 only in that the F-8 started at an initial altitude of 9144 m at Mach 0.5 and the target was flying at an altitude of 6048 m at Mach 0.74. Case 3 was completely different; the F-8 and the target were adjacent to each other but heading in opposite directions. They started at the same altitude separated by approximately one turn radius for the F-8.

The first case was chosen to demonstrate the aspects of a standard intercept without a lot of maneuvering required. Typically the F-8 initiated a gentle climbing

---

<sup>1</sup>The authors would like to acknowledge the contribution of Susan Carzoo of the Sperry Corporation to this paper. Her diligence went beyond what we could normally expect and allowed us to run the simulation in a useful and timely manner.

turn to the left to intercept the projected end point of the target trajectory, climbed to an efficient altitude for speed, and then descended to intercept the target. The second case had the F-8 at a high altitude and low velocity to demonstrate the algorithms' direction of a typical low-speed maneuver, consisting of a dive to gain speed and then a climb back to an efficient altitude for fast cruise. Case 3 was chosen to demonstrate the performance of the algorithms when hard maneuvers are called for. The pilot was required to make a hard 180° turn initially to chase the target. The F-8's initial velocity was higher than the optimal turning velocity at that altitude, so the algorithms directed the pilot to climb during the first part of the turn and then dive to gain speed. This is a typical high-speed yo-yo maneuver. Since the algorithm called for a 5g turn, which was the maximum g-loading allowed, the maneuver was difficult to perform - especially in a fixed-base cockpit.

Intercepts were flown with these three sets of initial conditions for combinations of three display modes and two optimization modes. The three display modes refer to the information shown to the pilot on the horizontal and vertical crossbars of the standard attitude indicator instrument used in the simulator. The information displayed in each of the three display modes is shown in table I. In each mode the pilot was to fly the simulated aircraft in a manner that would keep the needles centered in the attitude indicator instrument. Therefore, the instrument indicated the differences between the actual and desired values of the respective quantities as computed by the intercept algorithms.

Two optimization modes were used to compute the commands used to drive the vertical and horizontal display needles. The first optimization mode, called the suboptimal mode, used singular perturbations to compute a feedback control based on the four states: horizontal displacements  $x$  and  $y$ , total energy per unit weight  $E$ , and heading  $\beta$ , but used a proportional control law for the control relating altitude and flight-path angle dynamics, as discussed previously in the section on proportional vertical lift. The second optimization mode, called the fully optimal mode, used singular perturbation theory to compute a feedback control based on separating all six state variables, including altitude and flight-path angle. The proportional vertical lift control was always used for descent because during descent the F-8 is flying away from a stable equilibrium condition (cruise) and small errors at the top of descent would be magnified at the intercept point.

Nine pilots flew a total of eleven sets of data, and one pilot flew a partial data set. Two of the pilots flew two data sets each on different days. A full data set was comprised of 15 nonredundant combinations of initial conditions, display modes, and optimization modes. Since the third display mode did not use information that was unique to the fully optimal computation mode, that combination was not flown. The pilots were all active duty Air Force pilots currently flying F-15's or F-106's or, in one case, an active reserve pilot who was also currently flying F-106's. They were each allowed to fly the simulator for a few minutes to get the feel of the controls and instruments before data runs were begun.

The data recorded for each piloted flight consisted of the data necessary to describe the case being flown (initial conditions, optimization mode, and display mode), the time required to fly the intercept, and the computed distance from the target at the time of closest approach to the target. The data run was terminated when the F-8 passed the target and the range to the target started increasing, rather than decreasing. Out of 172 data runs recorded, 10 were eliminated because the minimum distance to the target was over 500 m. It was decided that these would not be called intercepts since the average final range for the remaining flights was well under 100 m.

## Discussion of Example Data Runs

Figures 8-13 show example piloted data runs for cases 1 and 3. Figure 8 shows the ground tracks generated by the F-8 and the target for case 1 with the fully optimal computation mode (mode 2) and display mode 1 (load factor on the horizontal needle and bank angle on the vertical needle). The F-8 starts at (0,0) on the plot and flies to intercept the target, which is flying at constant velocity. The curves in the F-8's path at the beginning and end of the flight are due to the initial change in heading and to heading corrections during the descent phase of the intercept.

Figure 9 shows altitude versus time for the same case. The curve marked by small squares represents the altitude command generated by the first boundary layer equations. Since altitude is considered control-like in these computations, jumps in altitude are allowed. The vertical jump in this curve at about 30 seconds into the flight occurs because the outer layer has at that point computed a new pseudo-cruise altitude for the F-8 based on its current position. This occurred because the F-8 was lagging the reference altitude during climb, thus traveling faster than it should have at all energy levels, and closing range with the target at a faster pace than appropriate for the climb path. Finally, the range to the target became sufficiently shortened that it became necessary to range-match to a lower pseudo-cruise energy level. Another large vertical step in altitude occurs at the beginning of descent as the first boundary layer equations shift to the descent path from the climb-cruise arcs. The lift computations take into account the dynamics in altitude and flight-path angle and thereby smooth the step changes that appear in the first boundary layer output.

The other curve in figure 9, which is marked by small circles, represents the actual altitude of the F-8 during the intercept. It can be seen that this curve has none of the step changes in altitude that occurred in the first boundary layer output. The actual altitude lags behind the reference altitude from the first boundary layer during the climb portion of the flight. This occurs because the control solution is based on a zero-order singular perturbation analysis, which results in a type zero control law. Hence, a nearly constant error results when following the ramp-like altitude reference during climb. Inclusion of first-order correction terms in the control solution would eliminate these errors.

Figure 10 shows altitude versus velocity for the same data run. The flight starts on the left-hand side of the figure. The F-8 initially (after a slight deceleration during the initial turn maneuver) picks up velocity without gaining much altitude. Then when the velocity has reached about 320 m/sec, the F-8 climbs from 3500 to 5500 m while the velocity decreases slightly. After one more jog in altitude as Mach 1 is passed, the F-8 accelerates to the high-speed point for this flight. At descent initiation, the algorithm directed the pilot to cut the throttle, roll the aircraft 180°, and pull back on the stick to start the descent as quickly as possible. In this particular case, the pilot pulled back on the throttle and matched the desired throttle indicator before rotating the aircraft and starting descent. This caused the F-8 to slow down significantly at constant altitude before beginning the descent. The F-8 then righted itself and flew down the  $q_{\max}$  boundary to the intercept point.

As noted earlier, figure 4 illustrates that when descent is initiated from sufficiently high cruise energies, the initial portion of the descent path should be flown at maximum thrust. Since this portion is relatively short in duration, it was decided to use equation (74) from the start of descent for the cases described in the paper. However, in retrospect, it seems that a better approach would have been to

delay the use of equation (74) until the aircraft velocity falls below the cruise velocity. This should result in a nearly constant-energy dive to the  $q_{\max}$  boundary in figure 10, rather than the initial deceleration at constant altitude.

It is interesting to compare the figures of this paper, for piloted flights, with figures from reference 2, for computer-generated non-piloted flights. Representative figures from reference 2 are presented in the appendix. Figures 8-10 may be compared with figures A1-A3. Curve 3 in the appendix figures represents the same initial conditions as case 1 flown here, but with no pilot in the loop. The differences between the two sets of figures are the result of pilot input. In the reference, perfect F-8 maneuvers were simulated based on the equations programmed for the aircraft, while the pilot flying the cases in the present study is following the visual commands shown on the cockpit instruments. Figure A3 actually represents a longer range intercept than the one flown here, but the characteristics of the shorter range case are similar.

Figures 11-13 are ground tracks, altitude versus time, and altitude versus velocity for case 3. These figures correspond to figures A4-A6 in the appendix except that for the piloted simulation the commands displayed were based on the sub-optimal optimization mode rather than the fully optimal mode. The suboptimal mode uses a proportional control law to compute commands based on the altitude and flight-path angle equations of motion, instead of using the commands generated exclusively by singular perturbations. For this reason, the lag between the reference and actual altitudes that was visible in the previous case and is visible in figure A5 does not appear in figure 12. Display mode 1 (load factor and bank angle) was again used for this data run. The computer-generated flights in reference 2 differed more from the piloted ones shown here because this case was very difficult for the pilots to fly. This case does demonstrate that the algorithms direct the pilot to fly a standard maneuver called a high-speed yo-yo in order to turn the F-8 around as quickly as possible. The algorithms direct the pilot to pull up as he starts the turn (at maximum g-loading) in order to slow the aircraft to the velocity for maximum turn rate. Then he is directed to dive again to gain speed as he approaches the proper heading for the intercept. The piloted runs show a much greater speed loss during the turning maneuver than do the computer-generated runs in reference 2.

Reference 10 contains a preliminary description of the piloted simulation described in this paper. It includes several example trajectories that are not included in this paper.

#### Discussion of Statistical Data From Piloted Runs

Tables II and III show statistics from the 162 data runs used for statistical analysis. These tables show the averages and standard deviations of the intercept times and intercept distances for the various optimization and display modes. Data are shown for all three sets of initial conditions. The standard deviations in intercept time for the three cases are shown in figure 14. The deviation for case 3 is over four times that of the other two cases.

The intercept times of the two pilots who each flew two full data sets are plotted against the order of those flights in figures 15-17. The vertical scales for these three plots have the same increments so that the slopes can be compared even though the average intercept times differed for the three cases. The plots for cases 1 and 2 show no significant decrease in intercept time as the pilots repeatedly flew the simulation runs. Therefore, variations in the data represent differences

due to the optimization and display modes chosen. However, for case 3, intercept times obviously decreased as the number of attempts at that case increased. This demonstrates that the pilots were still learning how to fly the intercept after 10 flights. The variations caused by different displays and optimization modes were generally small when compared with the improvement in intercept time as the pilots accumulated experience in flying the task. The difficulty of that particular case was attributed to the initial high-g 180° turn combined with vertical maneuvers. The pilots flying the simulator were all capable of performing such maneuvers successfully in an airplane. However, the combination of the side stick with force transducers and the lack of motion and out-the-window cues made flying this case very difficult.

Figure 18 shows that for the first two cases, the first display mode allowed for slightly better intercept times. Figure 19 shows that the second optimization mode (fully optimal) gave slightly better intercept times. The differences in intercept times caused by the display and optimization modes are small. However, intercept time is not the only consideration. Figure 20 shows that the intercept distance was greatly affected by the choice of display mode. Since the intercept distance is mainly determined by only the last part of the flight and is not influenced by the early part at all, the miss distance data from case 3 is valid. Thus, the data in figure 20 show the same trends for case 3 as the first two cases. These data show that the second display mode (heading and altitude rate) outperformed the other two consistently and that the third display mode (Mach number and heading) was by far the worst. This conclusion was supported by the pilots during the simulations. They found the third display mode very difficult to fly because of the very long lags between control inputs and responses of the indicator needles. There was no clear consensus among the pilots concerning the desirability of the first or second display mode.

#### Timing Considerations

Both the calculations needed to run the F-8 simulation and the onboard calculations required to use the algorithms were done by the CDC CYBER 175 computer system. To obtain an estimate of the time required to perform the onboard calculations, a timing routine was used under a number of different flight conditions with the display and control modes that required the most computations. The average time required by the onboard algorithms for all of these conditions was 1.2 msec, with a maximum time of 1.5 msec and a minimum of 1.1 msec. The memory required for the algorithms on the CDC computer was 47 744<sub>8</sub> 60-bit words. The number of words required for the programs themselves were 6773<sub>8</sub> with the rest going to storage (COMMON blocks). No attempt was made to optimize the program from the point of view of either time or memory requirements.

#### CONCLUDING REMARKS

This paper has presented algorithms for onboard computation of time-optimal intercept trajectories and described a piloted simulation of those algorithms. Singular perturbation techniques have been applied to that time-optimal intercept problem in order to simplify the problem for solution onboard the aircraft in real time. The feedback implementation of the solution has been described in detail.

A piloted simulation of the F-8 aircraft using the algorithms to generate controls for intercepting a moving target has demonstrated the feasibility of onboard



computation of optimal trajectories. Three sets of initial conditions (cases) for piloted simulations were chosen to demonstrate the capabilities of the algorithms and to determine the best information to display to the pilot. The data runs were made using two computation modes for the algorithms and three display modes for presenting information to the pilots. For statistical comparisons, 162 simulated intercepts were flown by 10 pilots.

Example data runs are shown that demonstrate the capabilities of the algorithms in the two computation modes and these runs are compared with previously published simulations which use the same algorithms but without a pilot in the loop. Information is included on the time required to compute the onboard calculations along with the storage requirements for the algorithms on CDC CYBER 175 computers.

The results of this simulation demonstrate that onboard computation of commands for time-optimal intercept is feasible. The pilots were able to use cockpit displays driven by the intercept algorithms to get very close to the target. Three different sets of parameters could be presented to the pilot for directing the intercept. The choice of display modes had little effect on the time required for intercept, but had a large effect on the minimum intercept distance. The best parameters to show the pilot, from the point of view of miss distance, were desired altitude rate and desired heading. Desired load factor and desired bank angle gave only slightly degraded performance.

For two sets of initial conditions (cases 1 and 2), the fully optimal computation mode, which used singular perturbation techniques to separate all the state variables, gave slightly better intercept times than the suboptimal mode, which relied on a proportional control law for the vertical lift command. The intercept time data for case 3 reflected the learning curve for the pilots as they learned to fly that very difficult case and was not useful for evaluating display or computation modes.

NASA Langley Research Center  
Hampton, VA 23665  
March 19, 1985

TABLE I.- INFORMATION DISPLAYED TO PILOT

Display mode	Vertical needle	Horizontal needle	Left-hand scale
1	Bank angle	Load factor	Throttle
2	Heading	Altitude rate	Throttle
3	Heading	Mach number	Throttle

TABLE II.- PARTIAL STATISTICS FOR INTERCEPT TIMES

Case	Statistic	Optimization mode		Display mode		
		Suboptimal	Fully optimal	1	2	3
1	Average, sec . . . . .	259.19	244.66	250.86	253.18	259.05
	Standard deviation, sec . . .	4.54	5.54	8.15	8.78	6.78
2	Average, sec . . . . .	275.50	269.99	269.20	275.95	276.27
	Standard deviation, sec . . .	7.87	6.32	6.78	6.57	8.32
3	Average, sec . . . . .	204.51	228.13	230.02	209.82	190.68
	Standard deviation, sec . . .	29.39	47.10	37.86	41.52	16.57

TABLE III.- PARTIAL STATISTICS FOR INTERCEPT DISTANCES

Case	Statistic	Optimization mode		Display mode		
		Suboptimal	Fully optimal	1	2	3
1	Average, m . . . . .	98.98	65.61	69.06	52.10	188.49
	Standard deviation, m . . . . .	92.43	48.69	47.74	21.63	116.08
2	Average, m . . . . .	85.39	72.07	71.91	56.18	152.96
	Standard deviation, m . . . . .	93.00	77.40	80.51	33.84	135.07
3	Average, m . . . . .	75.03	76.64	74.12	56.61	122.83
	Standard deviation, m . . . . .	91.23	96.60	93.65	86.85	91.33

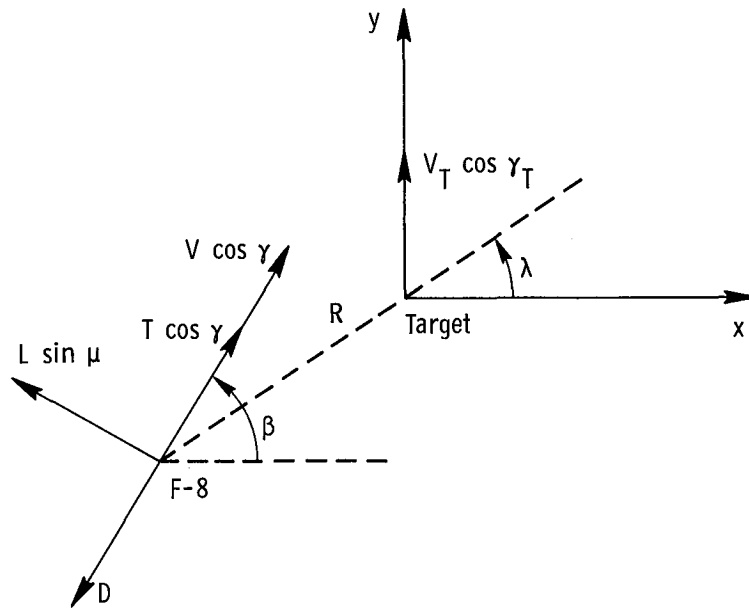


Figure 1.- Horizontal plane intercept geometry.

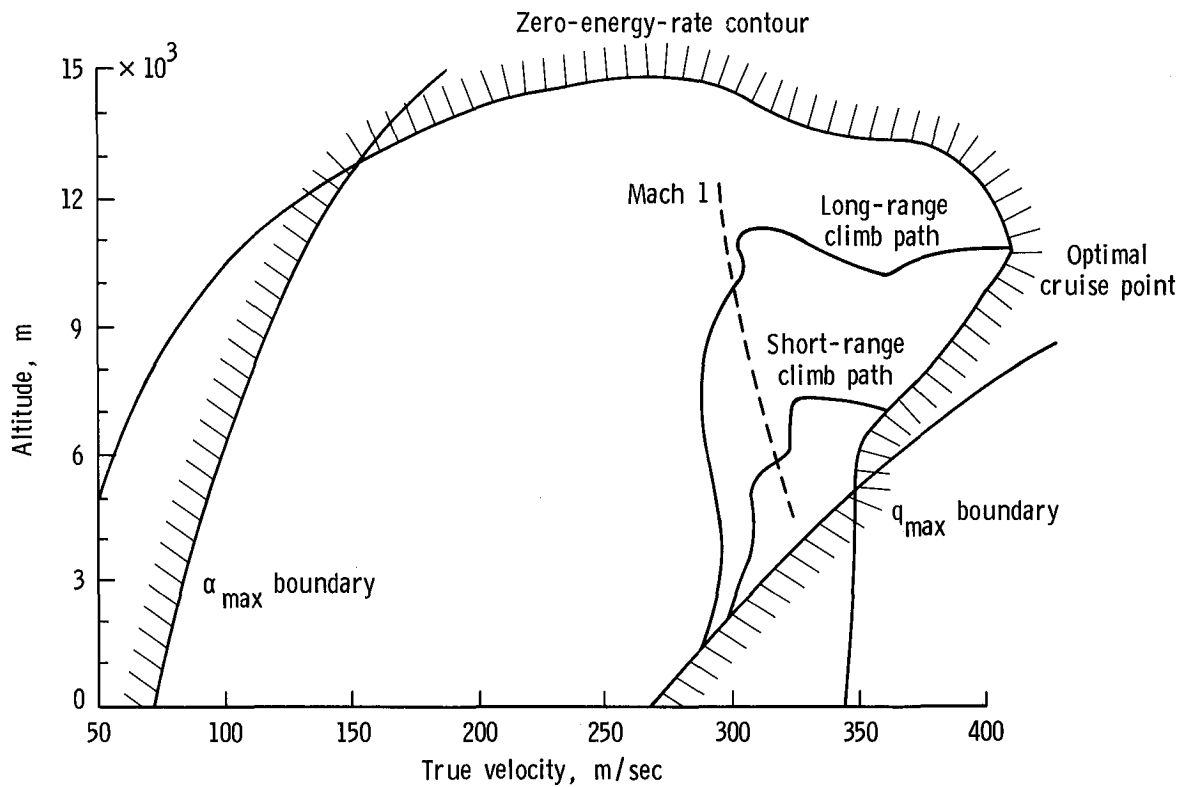


Figure 2.- Level flight envelope for F-8.

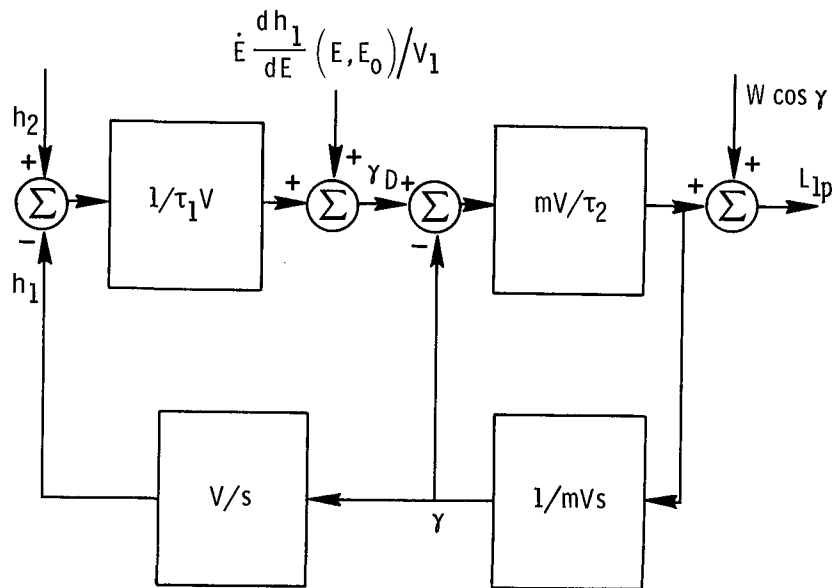


Figure 3.- Summary of control calculations of proportional vertical lift.

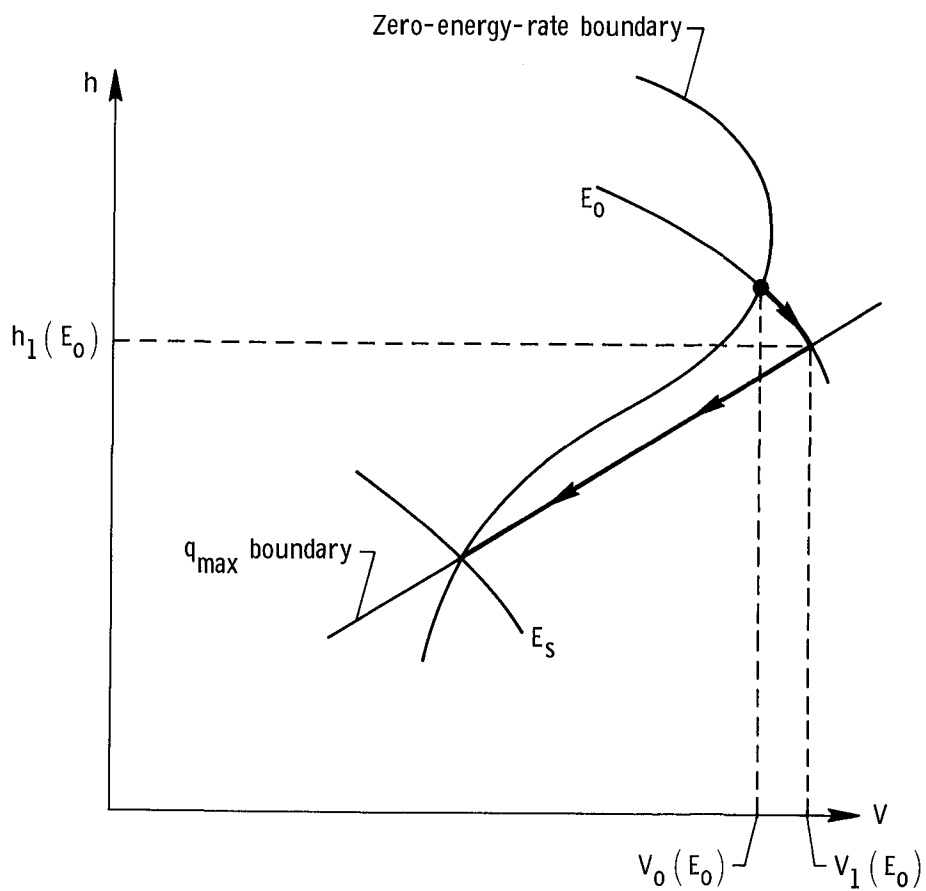


Figure 4.- Transition to descent.

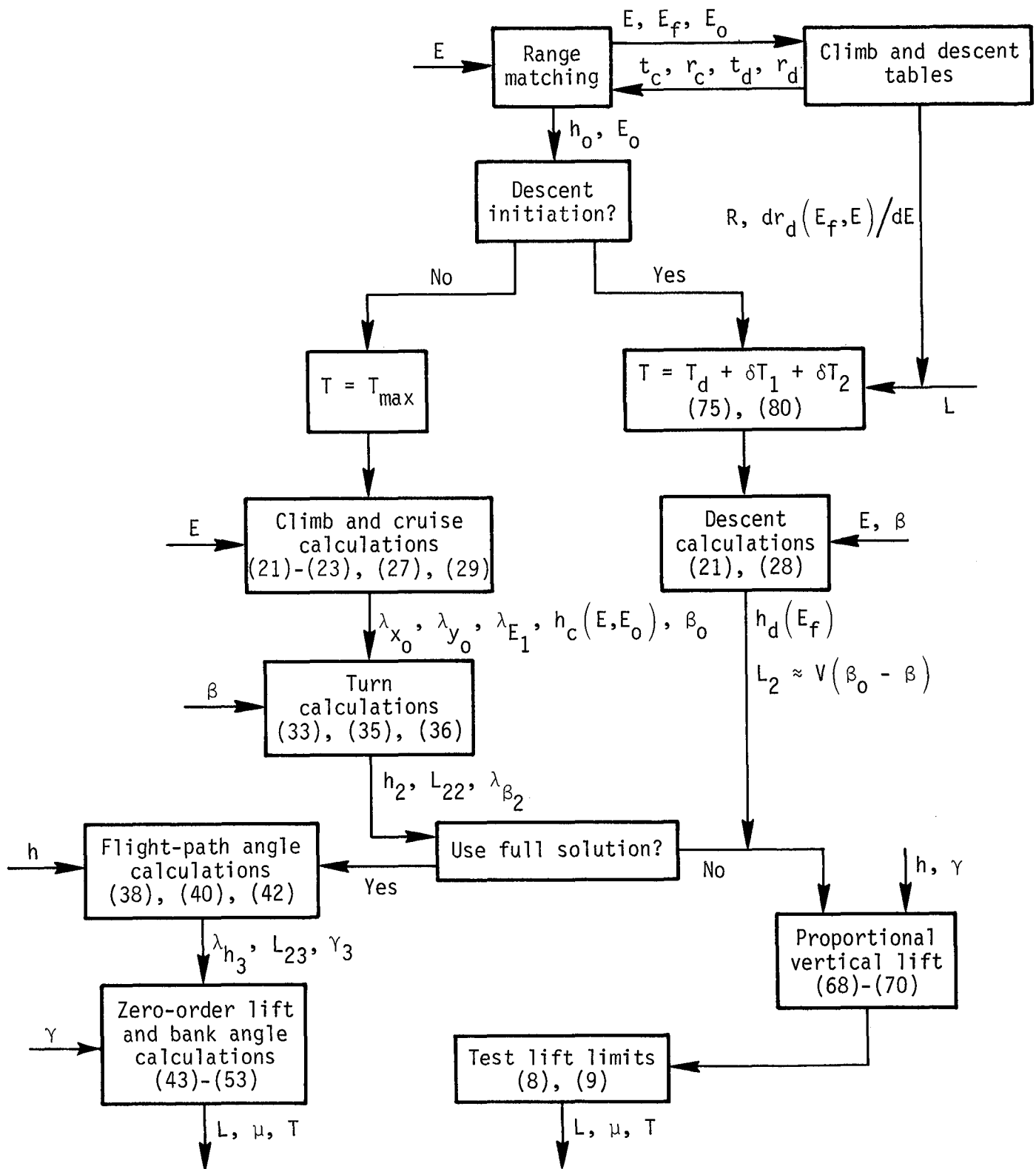


Figure 5.- Summary of control calculations. All on-line calculations are referenced by equation numbers.

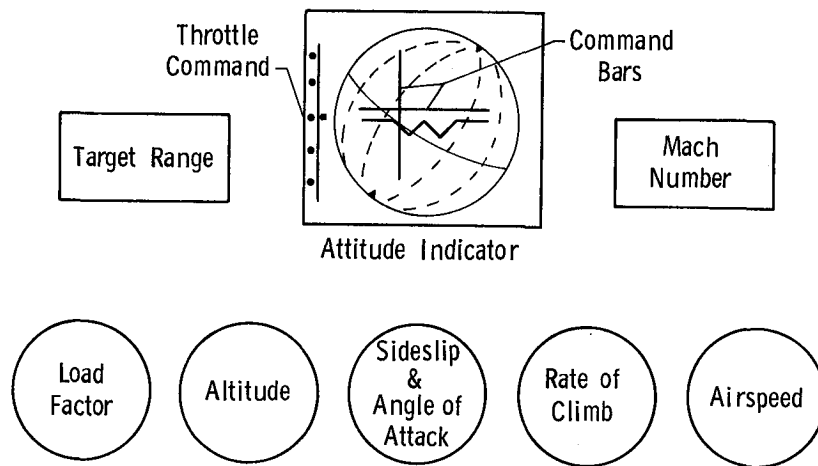
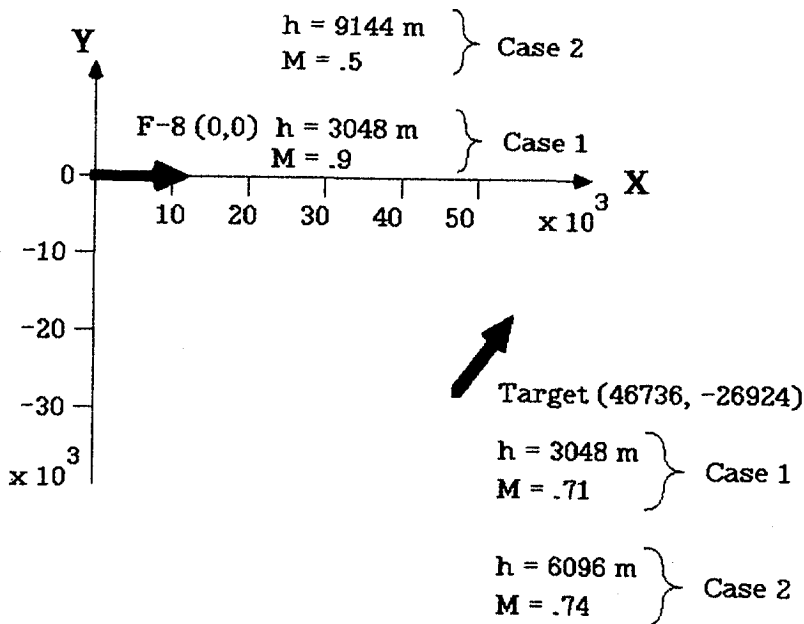


Figure 6.- Schematic of cockpit instrument panel.

## Initial Conditions:

### Cases 1 & 2



### Case 3

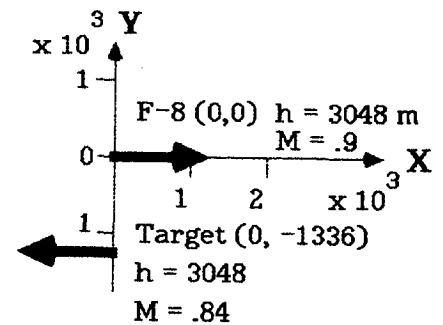


Figure 7.- Initial conditions for test cases.

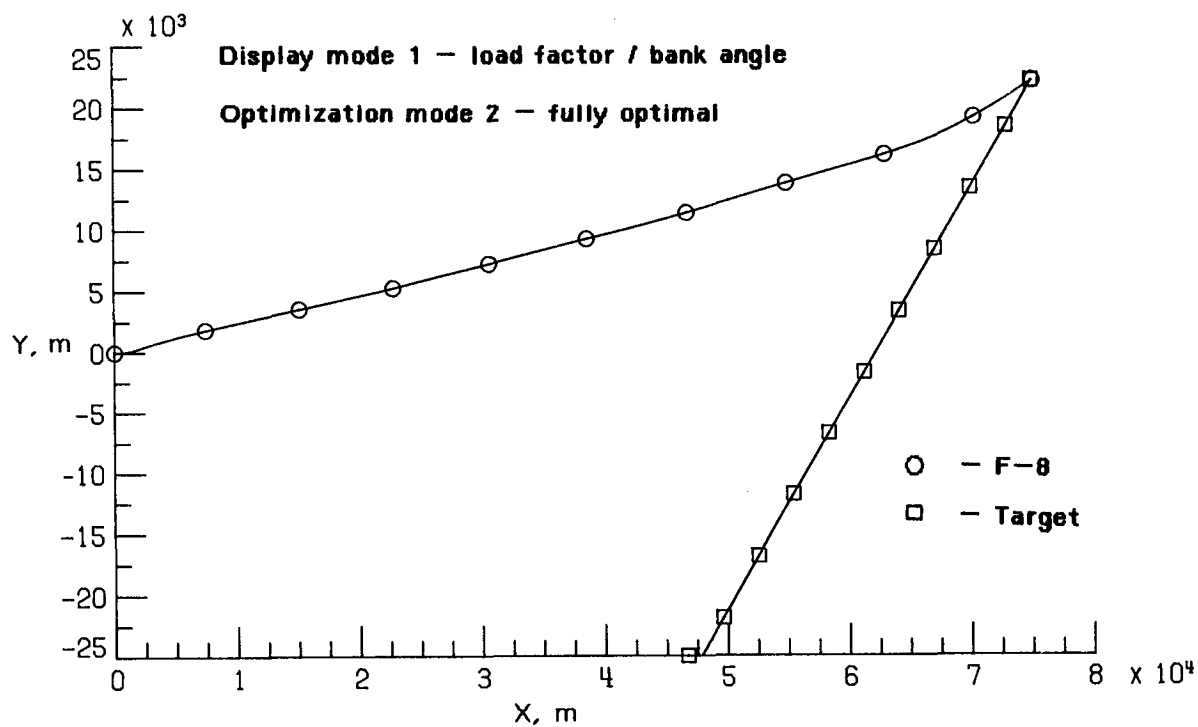


Figure 8.— Ground tracks for case 1.

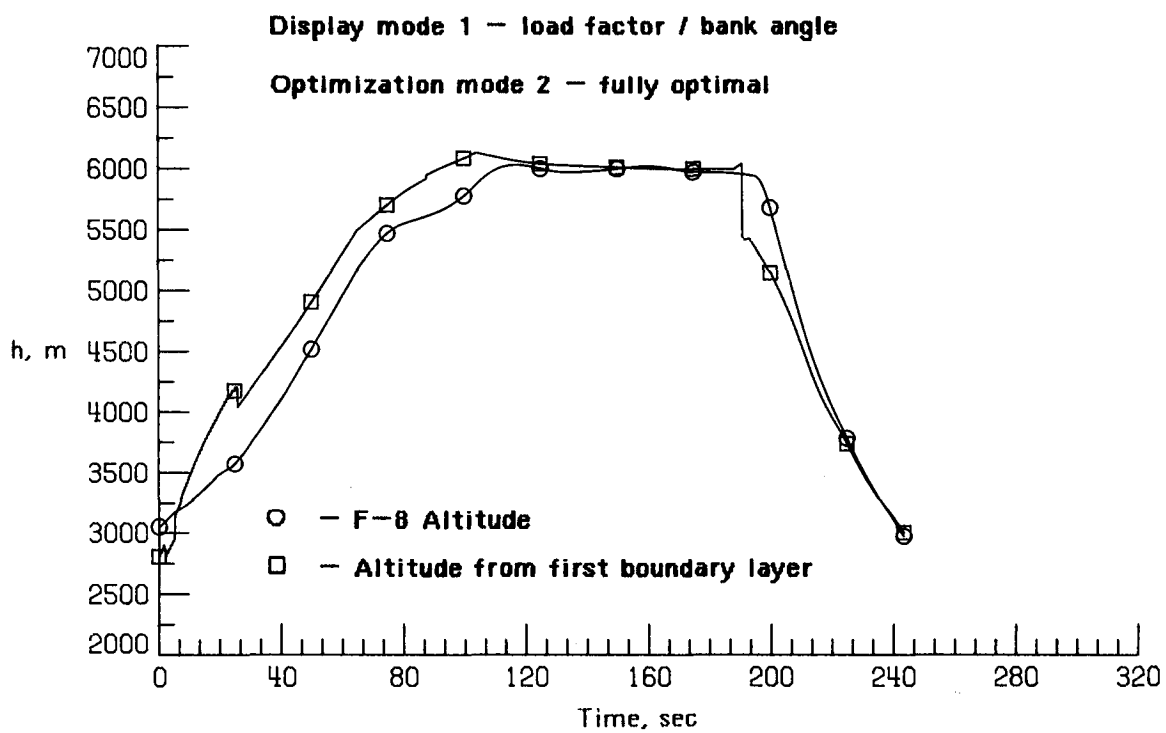


Figure 9.— Altitude versus time for case 1.

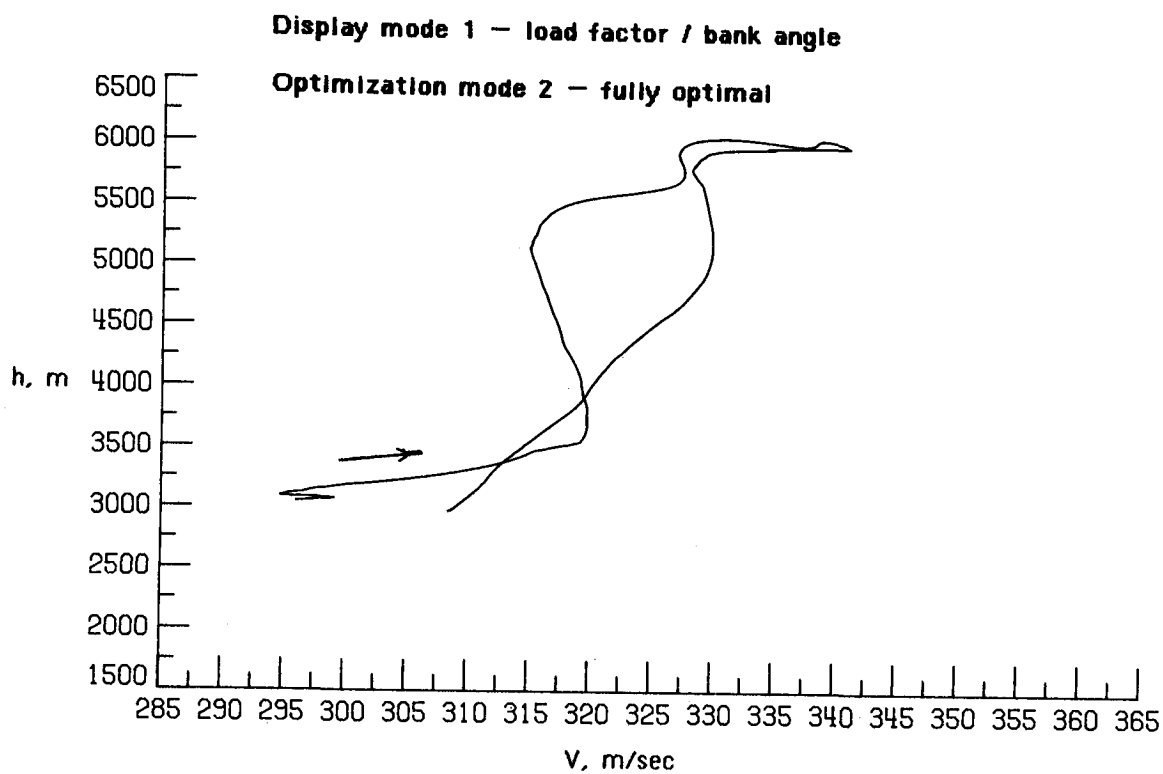


Figure 10.— Altitude versus velocity for case 1.

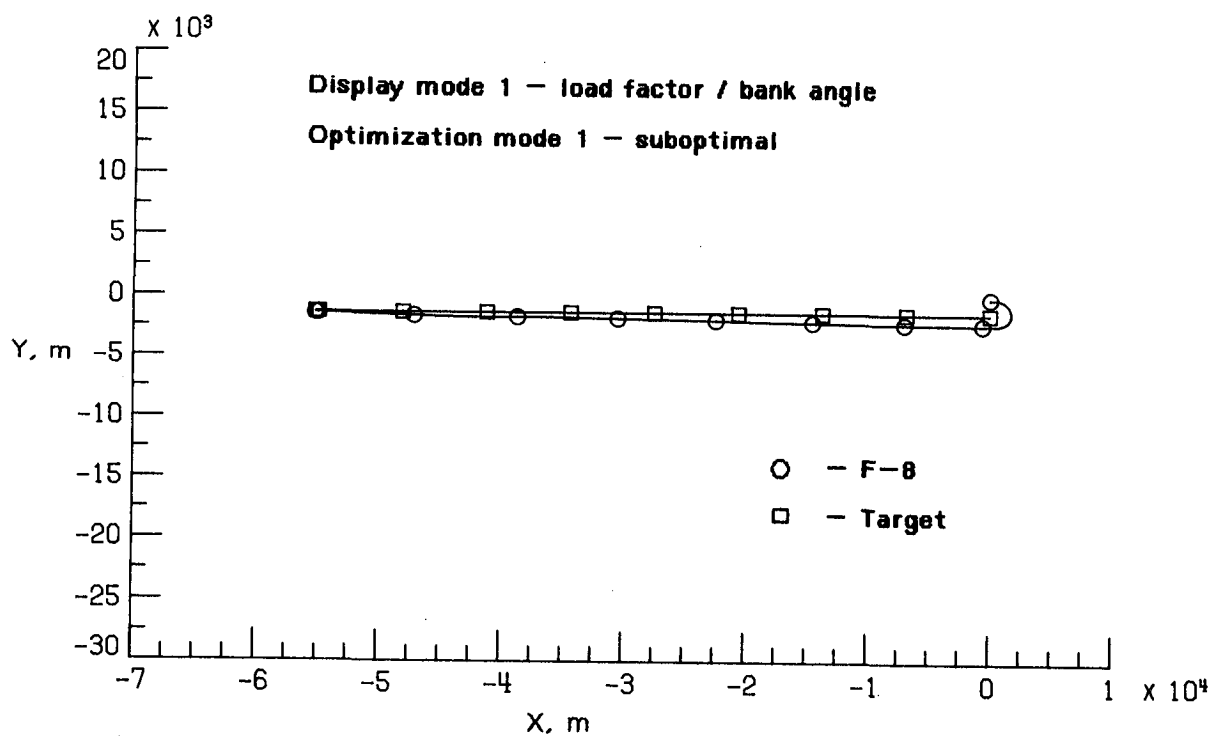


Figure 11.— Ground tracks for case 3.



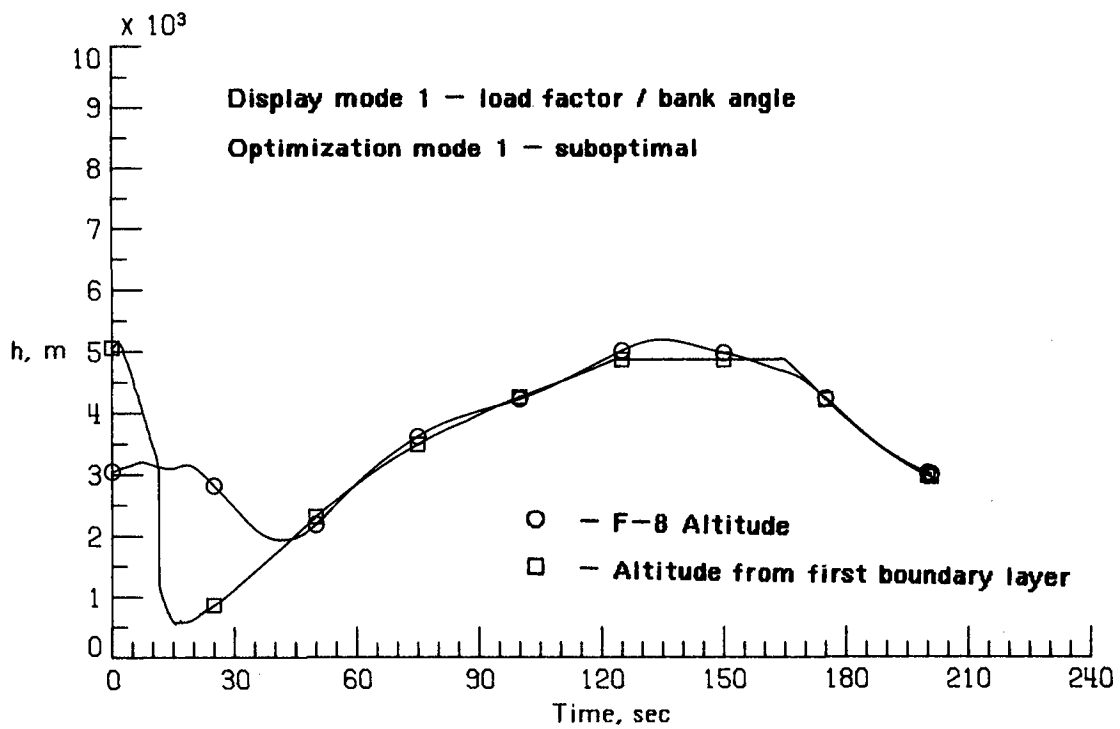


Figure 12.- Altitude versus time for case 3.

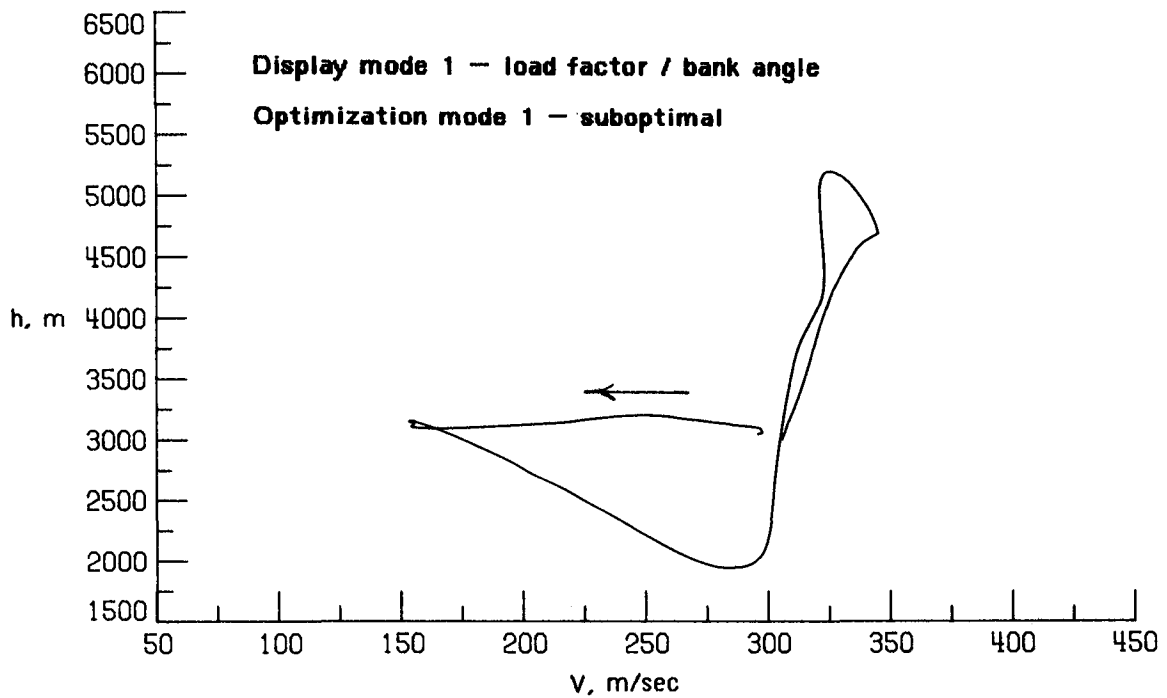


Figure 13.- Altitude versus velocity for case 3.

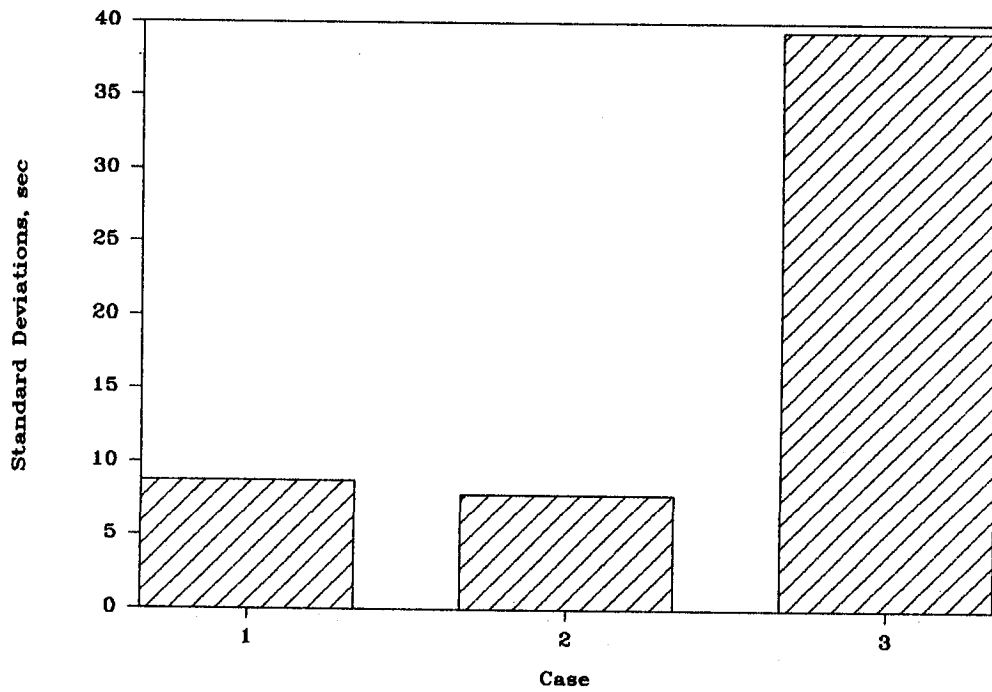


Figure 14.- Standard deviation of intercept times for three cases.

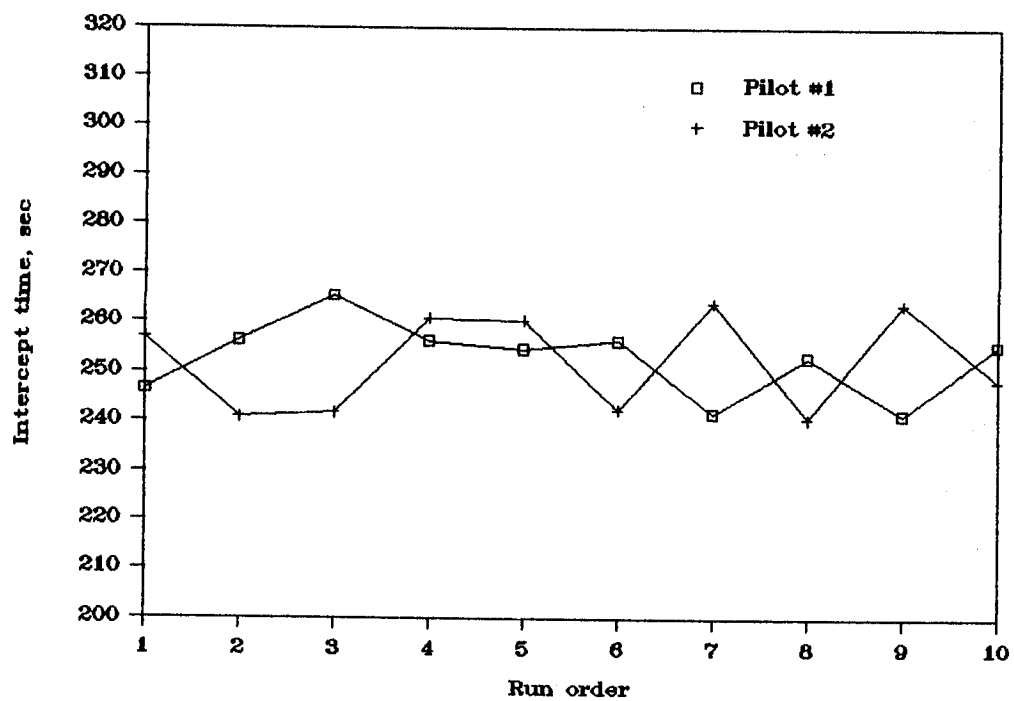


Figure 15.- Intercept time versus run order for case 1.

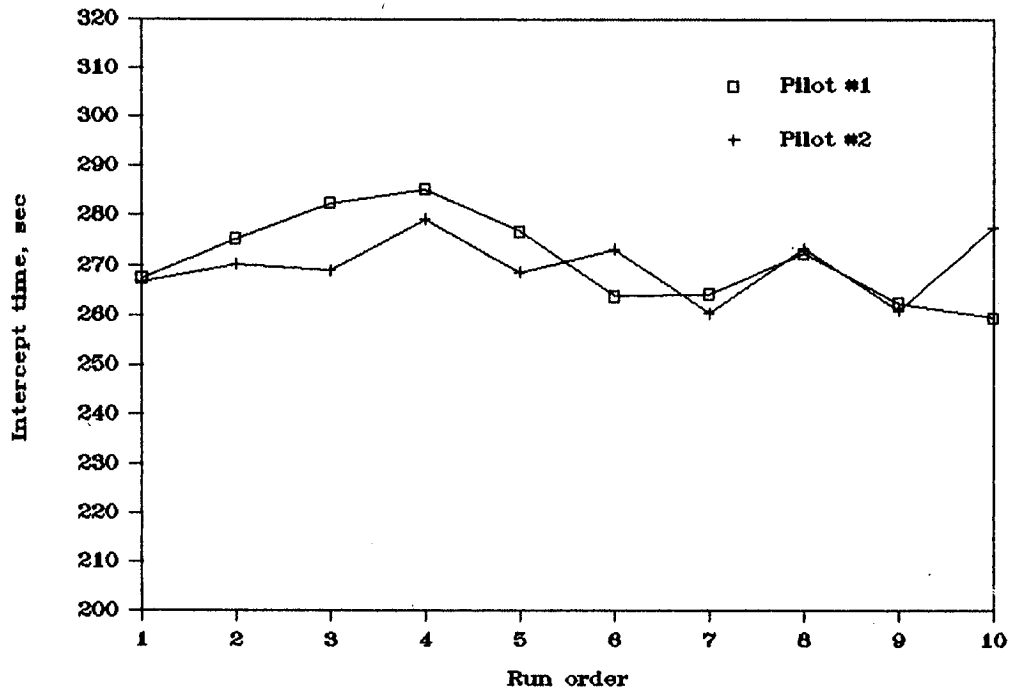


Figure 16.- Intercept time versus run order for case 2.

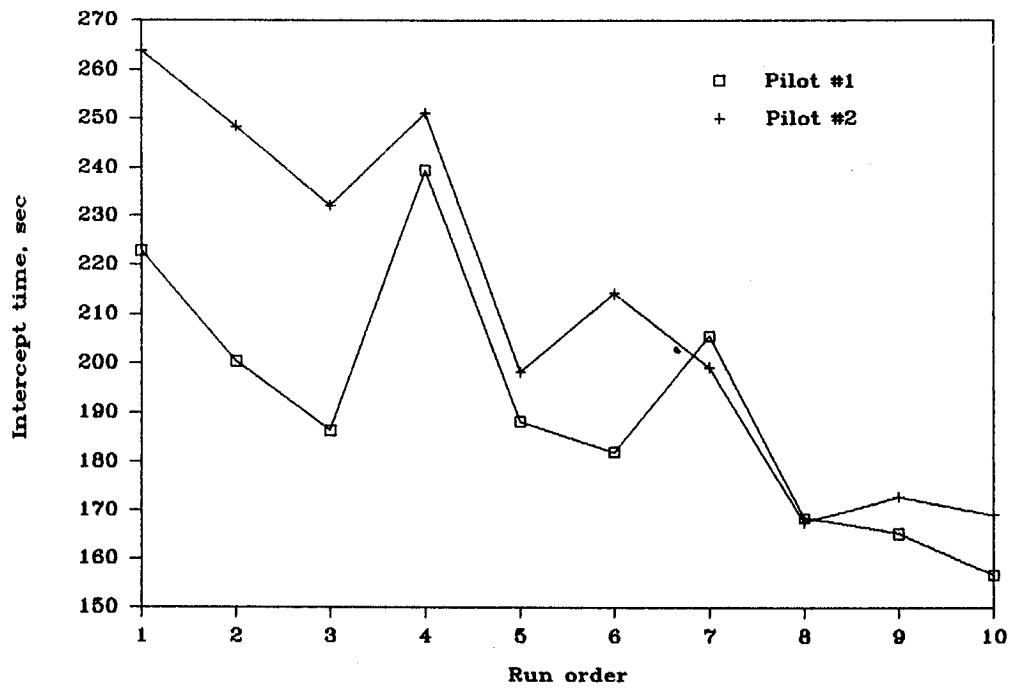


Figure 17.- Intercept time versus run order for case 3.

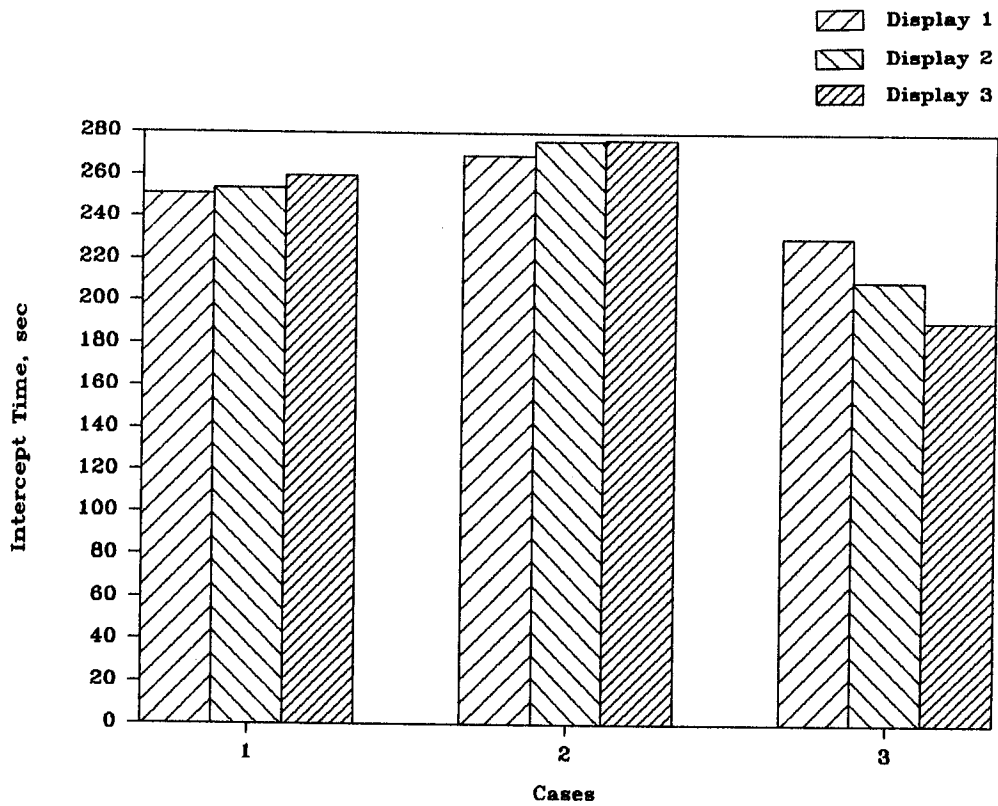


Figure 18.- Average intercept times for three display modes.

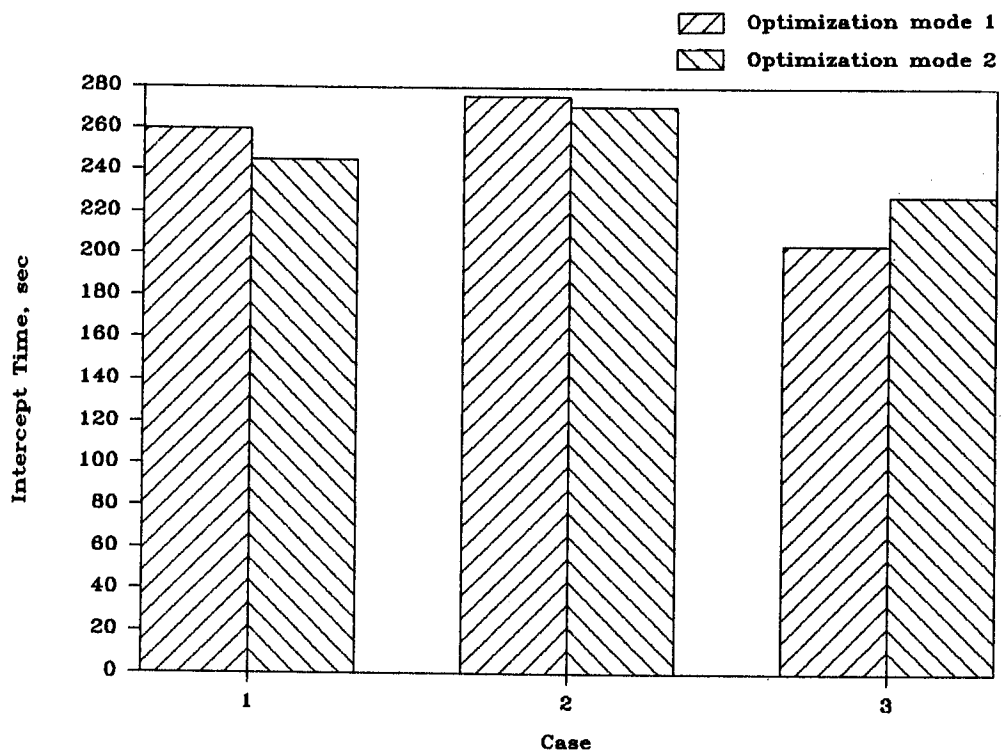


Figure 19.- Average intercept times for two optimization modes.

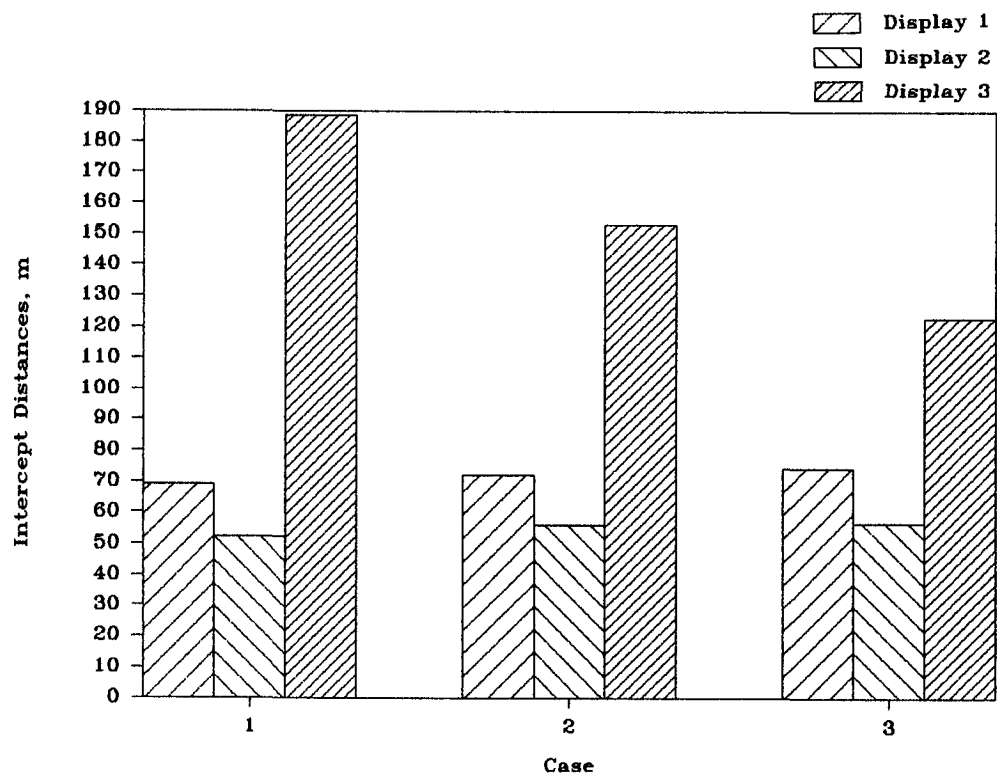


Figure 20.- Average intercept distances for three display modes.

# APPENDIX

## NON-PILOTED SIMULATION DATA FROM REFERENCE 2

This appendix presents figures 25-27 and figures 31-33 from reference 2, which are included for comparison with figures 8-13 of the present paper. The initial conditions for the simulations presented in figures A1-A6 are listed in table A1. Initial condition 3 in figures A1-A3 corresponds to case 1 in figures 8-10 and initial condition 4 in figures A4-A6 correspond to case 3 in figures 11-13.

TABLE A1.- INITIAL CONDITIONS FROM REFERENCE 2

Initial condition	x, m	y, m	h, m	$\beta$ , rad	V, m/sec
F-8 aircraft					
1	0	0	3048	0	295.92
2	0	0	3048	0	295.92
3	0	0	3048	0	295.92
4	0	0	3048	0	295.92
Target aircraft					
1	140 208	-80 772	3048	1.0472	232.56
2	93 023	-53 209	3048	1.0472	232.56
3	46 698	-27 000	3048	1.0472	232.56
4	0	1 335.7	3048	3.1416	274.32

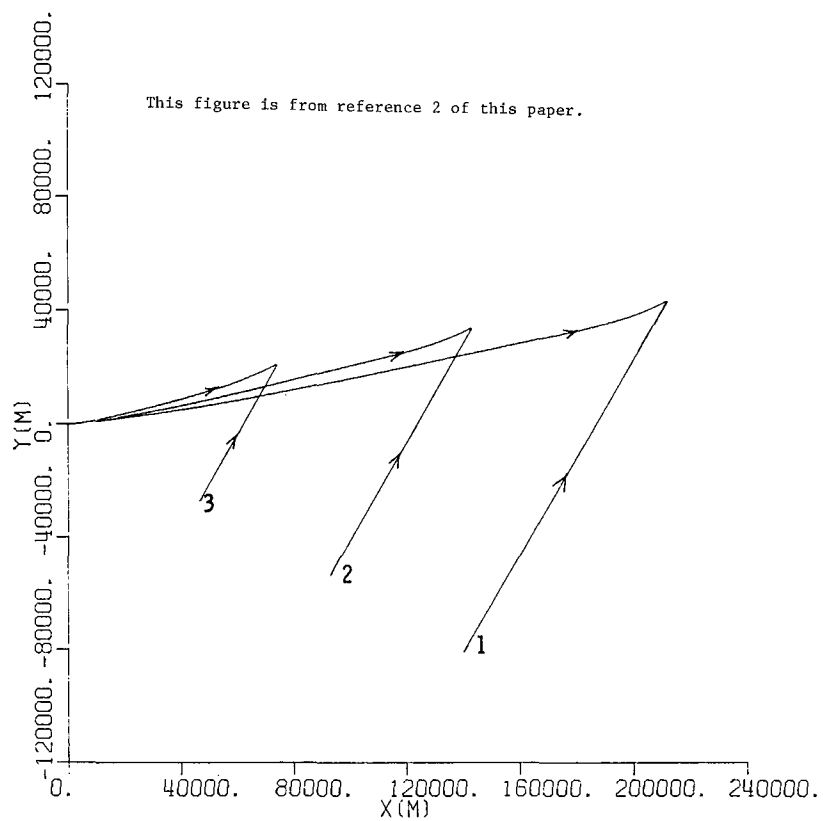


Figure A1.- Ground tracks for initial conditions 1-3.

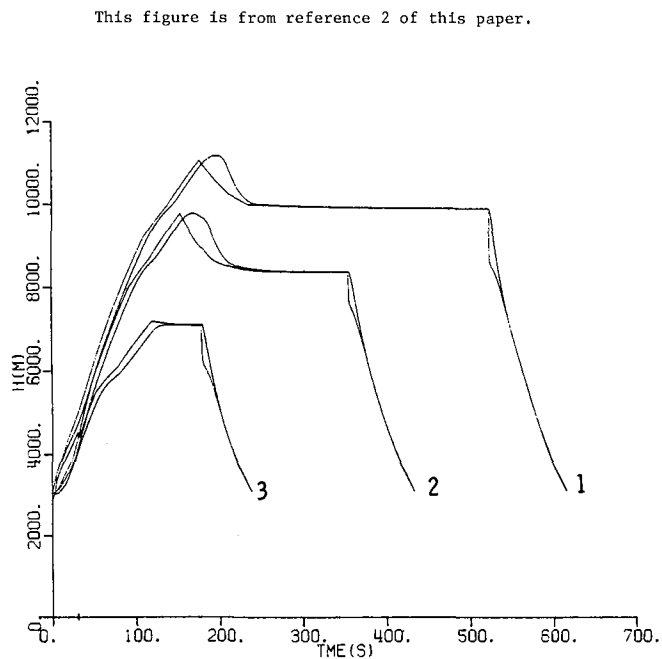


Figure A2.- Command and actual altitude profiles for initial conditions 1-3.

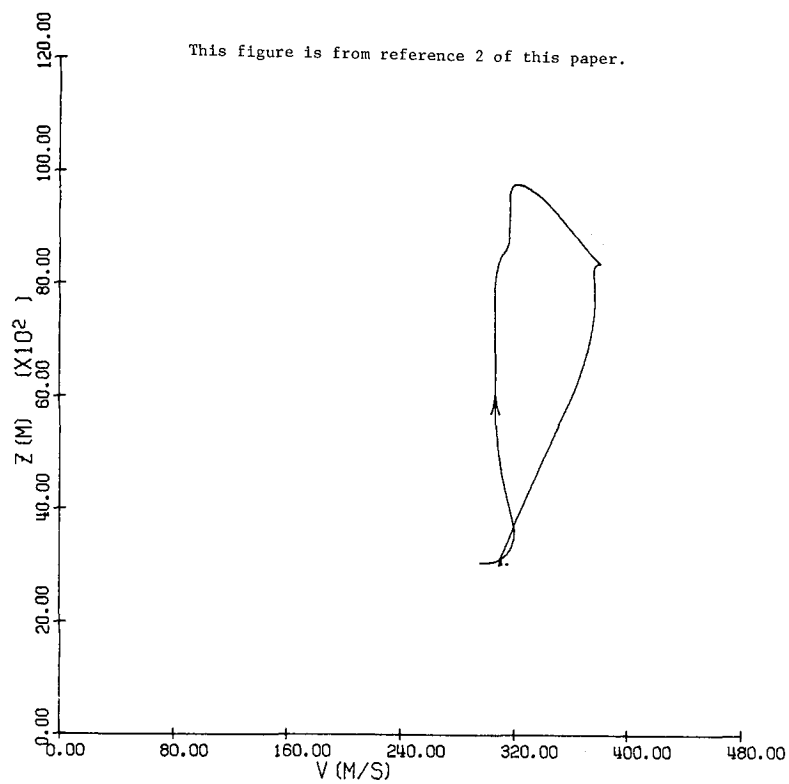


Figure A3.- Altitude versus velocity for initial condition 2.

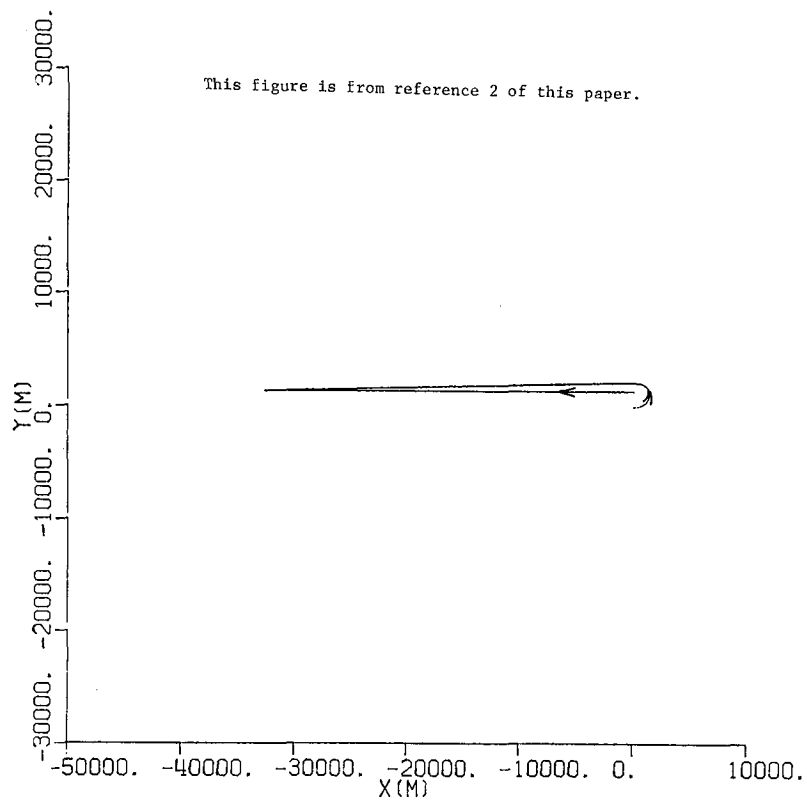


Figure A4.- Ground track for initial condition 4.



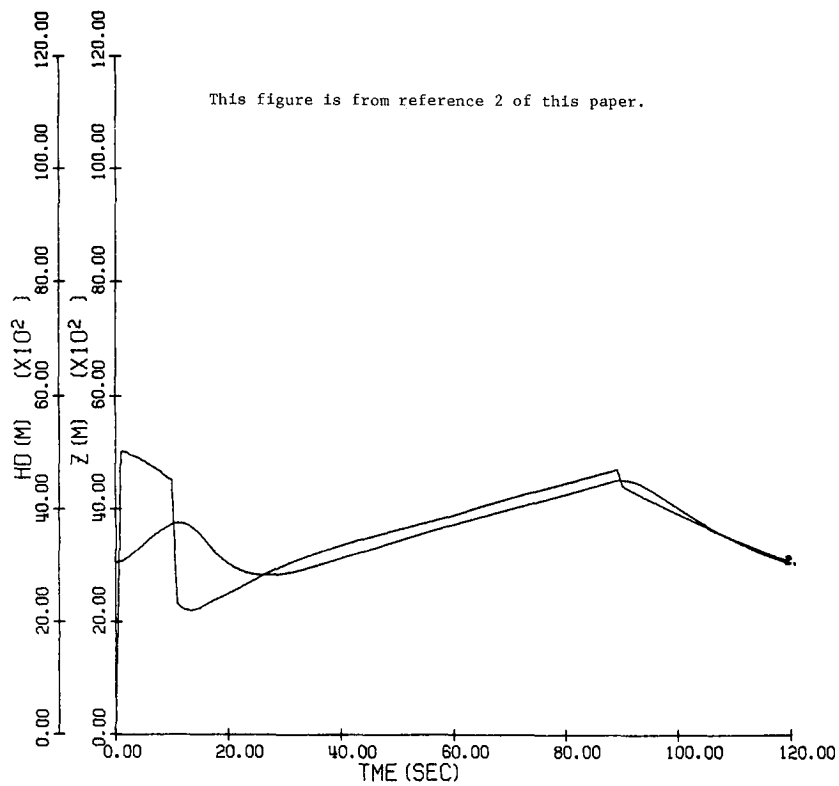


Figure A5.- Command and actual altitude profile for initial condition 4.

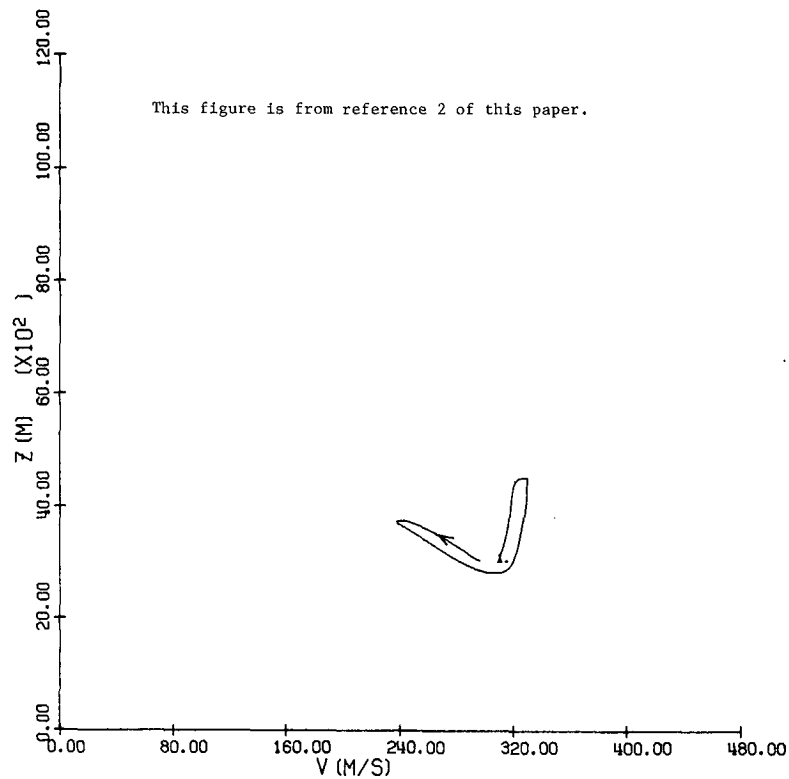


Figure A6.- Altitude versus velocity for initial condition 4.

## REFERENCES

1. Mehra, Raman K.; Washburn, Robert B.; Sajan, Salim; and Carroll, James V.: A Study of the Application of Singular Perturbation Theory. NASA CR-3167, 1979.
2. Calise, Anthony J.; and Moerder, Daniel D.: Singular Perturbation Techniques for Real Time Aircraft Trajectory Optimization and Control. NASA CR-3597, 1982.
3. Calise, Anthony J.: On-Line Optimization of Aircraft Altitude and Flight Path Angle Dynamics. Proceedings of the 1981 Joint Automatic Control Conference, Volume 1, American Automatic Control Council, 1981, Paper TA-1B.
4. Saksena, V. R.; O'Reilly, J.; and Kokotovic, P. V.: Singular Perturbations and Time-Scale Methods in Control Theory: Survey 1976-1983. Automatica, vol. 20, no. 3, May 1984, pp. 273-293.
5. Ardema, Mark D.: Solution of the Minimum Time-to-Climb Problem by Matched Asymptotic Expansions. AIAA J., vol. 14, no. 7, July 1976, pp. 843-850.
6. Calise, Anthony J.: A Singular Perturbation Analysis of Optimal Aerodynamic and Thrust Magnitude Control. IEEE Trans. Autom. Control, vol. AC-24, no. 5, Oct. 1979, pp. 720-730.
7. Chakravarty, Abhijit J. M.; and Vagners, Juris: Development of 4-D Time-Controlled Guidance Laws Using Singular Perturbation Methodology. Proceedings of the 1982 American Control Conference, American Automatic Control Council, 1982, pp. 1107-1108.
8. Calise, Anthony J.: Extended Energy Management Methods for Flight Performance Optimization. AIAA J., vol. 15, no. 3, Mar. 1977, pp. 314-321.
9. Calise, Anthony J.: Optimal Thrust Control With Proportional Navigation Guidance. J. Guid. & Control, vol. 3, no. 4, July-Aug. 1980, pp. 312-318.
10. Price, Douglas B.; Calise, Anthony J.; and Moerder, Daniel D.: Piloted Simulation of an Onboard Trajectory Optimization Algorithm. J. Guid., Control, & Dyn., vol. 7, no. 3, May-June 1984, pp. 355-360.







1. Report No. NASA TP-2445		2. Government Accession No.		3. Recipient's Catalog No.	
4. Title and Subtitle Piloted Simulation of an Algorithm for Onboard Control of Time-Optimal Intercept				5. Report Date June 1985	
				6. Performing Organization Code 505-34-03-02	
7. Author(s) Douglas B. Price, Anthony J. Calise, and Daniel D. Moerder				8. Performing Organization Report No. L-15896	
9. Performing Organization Name and Address  NASA Langley Research Center Hampton, VA 23665				10. Work Unit No.	
				11. Contract or Grant No.	
12. Sponsoring Agency Name and Address National Aeronautics and Space Administration Washington, DC 20546				13. Type of Report and Period Covered Technical Paper	
				14. Sponsoring Agency Code	
15. Supplementary Notes Douglas B. Price: NASA Langley Research Center, Hampton, Virginia. Anthony J. Calise: Drexel University, Philadelphia, Pennsylvania. Daniel D. Moerder: Information and Control Systems, Inc., Hampton, Virginia.					
16. Abstract  This paper describes a piloted simulation of algorithms for onboard computation of trajectories for time-optimal intercept of a moving target by an F-8 aircraft. The algorithms, which were derived using singular perturbation techniques, generate commands which are displayed to the pilot on the command bars of the attitude indicator in the cockpit. By centering the horizontal and vertical needles, the pilot flies an approximation to a time-optimal intercept trajectory. Several example simulations are shown and statistical data on the pilot's performance when presented with different display and computation modes are described.					
17. Key Words (Suggested by Author(s))  Trajectory optimization      Simulation Minimum-time control Model order reduction Perturbation methods Flight control algorithms				18. Distribution Statement  Unclassified - Unlimited   Subject Category 08	
19. Security Classif. (of this report) Unclassified	20. Security Classif. (of this page) Unclassified	21. No. of Pages 47	22. Price A03		



National Aeronautics and  
Space Administration

Washington, D.C.  
20546

Official Business

Penalty for Private Use, \$300

THIRD-CLASS BULK RATE

Postage and Fees  
National Aeronautics and  
Space Administration  
NASA-451

3 1176 01311 2975



**NASA**

POSTMASTER: If Undeliverable (Section 158  
Postal Manual) Do Not Return

---